JAMES | Journal of Advances in Modeling Earth Systems

RESEARCH ARTICLE
10.1029/2022MS002989

The Representation of Spiral Gravity Waves in a Mesoscale Model With Increasing Horizontal and Vertical Resolution

David S. Nolan[1] **and Matthew J. Onderlinde**[2]

[1]Rosenstiel School of Marine and Atmospheric Science, University of Miami, Miami, FL, USA, [2]National Hurricane Center, Miami, FL, USA

Key Points:

- Computer simulations of tropical cyclones show the detailed structures of outward propagating spiral gravity waves
- As resolution increases, the wave properties come close to, but do not converge to observed values
- A new class of waves is identified in the upper-level outflow, which are slow-moving spiral waves due to dynamical instabilities

Supporting Information:

Supporting Information may be found in the online version of this article.

Correspondence to:

D. S. Nolan,
dnolan@miami.edu

Citation:

Nolan, D. S., & Onderlinde, M. J. (2022). The representation of spiral gravity waves in a mesoscale model with increasing horizontal and vertical resolution. *Journal of Advances in Modeling Earth Systems*, *14*, e2022MS002989. https://doi.org/10.1029/2022MS002989

Received 10 JAN 2022
Accepted 28 JUN 2022

Author Contributions:

Conceptualization: David S. Nolan
Data curation: Matthew J. Onderlinde
Formal analysis: David S. Nolan
Funding acquisition: David S. Nolan
Investigation: David S. Nolan
Methodology: David S. Nolan, Matthew J. Onderlinde
Project Administration: David S. Nolan
Software: Matthew J. Onderlinde
Supervision: David S. Nolan
Visualization: David S. Nolan
Writing – original draft: David S. Nolan

Abstract Recent observational and numerical studies have investigated the dynamics of fine-scale gravity waves radiating horizontally outward from tropical cyclones. The waves are wrapped into spirals by the tangential wind of the cyclone and are described as spiral gravity waves. This study addresses how well numerical simulations of these waves compare to observations as the horizontal grid spacing is decreased from 2.0 to 1.0 to 0.5 km, and the number of vertical levels changes from 25 to 50 to 100. Spectral filtering is applied to separate the fine-scale waves in vertical velocity (w) and the larger-scale waves in pressure (p) from moist updrafts and downdrafts in the eyewall and rainbands. As the grid spacing decreases, the radial wavelengths of the w waves decrease from 20 to 7 km, approaching observed values. For grid spacing 1.0 km, the p waves become well-resolved with wavelength 70 km. The outward phase speeds range from 15 to 30 ms^{-1} for the w waves and 50 to 70 ms^{-1} for p waves. Analysis of the upper-level outflow region finds that the spiral w waves propagate 5–10 ms^{-1} faster due to radial advection, but also finds what appear to be different classes of larger-amplitude, slow-moving spiral waves. Similar waves can be seen in satellite images, which appear to be caused by dynamical instability of the strongly vertically sheared radial and tangential winds in the TC outflow.

Plain Language Summary Tropical cyclones—known also as hurricanes, typhoons, and cyclones—cause some of the most significant weather impacts around the world. Recent work has found that these storms causes oscillations in the atmosphere that radiate outward in expanding spirals. These are called spiral gravity waves. This paper investigates how well computer models reproduce these waves as the pixel sizes used by the model become smaller (requiring more computer power). As the pixels decrease to 1.0 km or less, the waves become increasingly realistic. The simulations show two types of spiral gravity waves, which can be seen either in vertical motion or in the atmospheric pressure field. The vertical motion waves are 5–10 km wide and move outward at 90 km hr^{-1}, while the pressure waves are 60–80 km wide and move outward at 220 km hr^{-1}. Focusing on the cloud shield at the top of the cyclone (what we see in satellites) reveals a new class of slow-moving, spiral waves that are distinct from the gravity waves.

1. Introduction

Anthes et al. (1971) and Anthes (1972) presented some of the earliest attempts at three-dimensional numerical modeling of a tropical cyclone (TC). Despite using horizontal grid spacings of 30 km and only three model levels, the simulations did produce some of the desired features, such as low-level flow spiraling toward the center that abruptly rose to the tropopause, and then diverged outward into asymmetric patterns. Long spiral bands of enhanced precipitation were also evident, about 90 km wide, and propagating outward at 24 knots (12 m s^{-1}). Anthes (1972) explained that these were probably inertia-gravity waves and perhaps not correct representations of spiral rainbands in real TCs. Kurihara and Tuleya (1974) presented a three-dimensional simulation with 20 km grid spacing and 11 vertical levels. They also noted robust spiral bands of vertical motion, in their case propagating outward at 27 m s^{-1}, with temperature and vertical motion out of phase, thus consistent with gravity waves.

After those early attempts, the vertical and horizontal grid spacings of TC models steadily decreased while the realisms of their simulated TCs steadily increased (Braun et al., 2006; Liu et al., 1997; Rogers et al., 2003). The TC eye and eyewall became well-resolved while the spiral bands of precipitation became narrower and moved more slowly to the point where it can be difficult to differentiate their motion with that of the tangential circulation (Moon & Nolan, 2015a, 2015b). At the same time, vertical motions associated with gravity waves have become steadily less prominent in numerical simulations and have received accordingly less interest. An exception is the study by Chow et al. (2002), who analyzed outward propagating spirals in a Mesoscale Model 5 (MM5)

Writing – review & editing: David S. Nolan, Matthew J. Onderlinde

simulation of a TC with 5 km grid spacing. The vertical motions were quite small, on the order of 0.1 m s^{-1}. Chow and Chan (2003) suggested that such waves were continuously transporting substantial angular momentum out of the TC core, as much as 10% of the inner core angular momentum per hour. These claims were contradicted by Schecter (2008), Hendricks et al. (2010), and Moon and Nolan (2010) who all found drastically less angular momentum transport by gravity waves.

Nolan and Zhang (2017; hereafter NZ17) brought renewed consideration to spiral gravity waves (SGWs) radiating from TCs. They found that, in a mesoscale model simulation with a grid spacing of 1 km, the radial scales of the SGWs are much finer, 10 km or less, and they seem to be almost completely decoupled from spiral rainbands, often passing through them with little interaction. At the same time, NZ17 identified SGWs in the surface pressure field (p) with larger radial scales that are distinct from the finer scale waves in vertical velocity (w). NZ17 also presented in situ observations supporting these two classes of waves. The fine-scale w waves were inferred from flight-level observations by the NOAA P-3 aircraft, revealing their approximate radial wavelengths (4–8 km) and phase speed (about 22 m s^{-1}). The larger-scale p waves were inferred from surface pressure measurements in a research buoy placed in the West Pacific (Potter et al., 2015). The most prominent p oscillations had periods of 2,000–3,000 s, consistent with the simulated p waves, but their radial scales or speeds could not be independently deduced from solitary observations at fixed points.

Nolan (2020; hereafter N20) proposed that the primary source of SGWs is the pulsation of convective maxima in the TC eyewall as they are advected through the convectively enhanced, downshear-left quadrant of a TC. N20 tested this hypothesis by forcing a linear dynamical model of perturbations to a TC-like vortex with idealized heat sources that were rotating and pulsing. This forcing reproduced many of the features of the waves seen in NZ17, and it clarified the p waves and w waves as distinct from each other, being the results of the projection of the heat forcing onto different vertical and horizontal modes.

In this paper, we return to a more detailed assessment of SGWs in numerically simulated TCs. As the simulated waves of NZ17 appeared to be close to, but not matching, the observed radial wavelengths, it is reasonable to wonder whether decreasing the horizontal grid spacing will achieve the observed values. Increasing vertical resolution may also lead to more realistic behaviors. A consistent set of six simulations with varying horizontal and vertical resolution is presented, and an objective analysis of the radial and vertical scales of the w and p waves is performed. While most of the analysis focuses on motions near 700 hPa ("flight level") and at the surface, the final section of the paper looks at the w waves embedded in the upper-level outflow.

Table 1
Grid Sizes and Resolution for the Weather Research and Forecasting Model Simulations

Simulation name	Grid sizes	Grid spacings (km)	Vertical levels
GS2.0	360 × 240	18.0	50
	219 × 219	6.0	
	405 × 405	2.0	
GS1.5	480 × 321	13.5	50
	291 × 291	4.5	
	540 × 540	1.5	
GS1.0	240 × 160	27.0	50
	180 × 180	9.0	
	270 × 270	3.0	
	640 × 640	1.0	
GS0.5	480 × 321	13.5	50
	291 × 291	4.5	
	540 × 540	1.5	
	1200 × 1200	0.5	
L25	As in GS1.0	As in GS1.0	25
L100	As in GS1.0	As in GS1.0	100

2. Simulations

The idealized TC simulations in this study were produced using version 3.9.1.1 of the Weather Research and Forecasting Model (WRF). The vortex-following, multiplynested grid capabilities of the WRF model were used to create simulations having innermost nests with grid spacings of 2.0, 1.5, 1.0, and 0.5 km. Most of the simulations used 50 vertical levels between the surface and an upper boundary at approximately $z = 26$ km. The vertical distribution of levels is designed to have better resolution in the boundary layer and around the tropopause. A similar distribution is shown in Figure 2 of Nolan et al. (2013), except in that paper there are 60 levels between the surface and 20 km. The upper boundary is elevated here to 26 km to reduce its influence on upward and outward gravity wave propagation; in addition, the WRF upper-level damping scheme (Klemp et al., 2008) is activated above 20 km to limit gravity wave reflection. Using the 1 km inner nest arrangement, two additional simulations were performed with 25 vertical levels and 100 vertical levels between the surface and 26 km. Specific domain sizes and other features of the six simulations are shown in Table 1. For all simulations, the size of the outer domain is 6,480 × 4,320 km. The sizes of the innermost nests for the simulations named GS2.0, GS1.5, GS1.0, and GS0.5 are 810 × 810, 810 × 810, 640 × 640, and 600 × 600 km. The inner nest

of the 0.5 km simulation is very large: 1,200 × 1,200 grid points. For this reason it is initialized differently, as discussed below.

The initial atmospheric temperature and moisture profiles are based on the moist tropical sounding of Dunion (2011). However, the humidity is reduced by up to 10% in a layer between 700 and 400 hPa (see Figure 16 of Nolan & McGauley, 2012). This reduces convective activity in the outer core region, allowing the storms to contract to a smaller size, and reducing interference from rainbands at large radius. The large-scale wind field is easterly at 5 m s^{-1} between the surface and 850 hPa, smoothly decreases with height to easterly at 2.5 m s^{-1} at 200 hPa, and is constant above that. Thus there is effectively 2.5 m s^{-1} of westerly vertical wind shear. As discussed in NZ17 and N20, even this very weak vertical shear has a strong organizing effect on the eyewall asymmetries. Since persistent zero vertical wind shear never occurs in reality, simulations with zero wind shear and completely "isotropic" inner core asymmetries would be quite unrealistic.

The enforcement of the boundary conditions, control of the large-scale flow, and TC initialization procedure follow the "point-downscaling" (PDS) method of Nolan (2011). The PDS framework has been applied in many previous studies using idealized TC simulations (Dai et al., 2021; Hlywiak & Nolan, 2019; Onderlinde & Nolan, 2016; Rios-Berrios, 2020; Zhang & Tao, 2013). Rather than being balanced by a meridional pressure force and meridional temperature gradients as required by the thermal wind equation, the initial large-scale flow is held in balance by an artificial pressure gradient force, selected to match the initial wind profile as a function of height. This allows the initial atmospheric sounding to be constant across the domain, and also allows for doublyperiodic boundary conditions on the outer grid. This effectively places the simulated TC on an infinite ocean surrounded with an atmosphere of constant sounding and wind profile. The Coriolis parameter is set to the constant value $f = 5.0 \times 10^{-5}$ s^{-1}. Microphysical processes are parameterized with the WRF 6-class, single-moment scheme (WSM6; Hong & Lim, 2006) and the Yonsei University scheme (Hong et al., 2004) is used for the boundary layer. To prevent drift in the large-scale sounding and disruptions by the diurnal cycle (Dunion et al., 2014; O'Neill et al., 2017), the longwave and shortwave radiation schemes are not activated. Without radiative cooling, the domain-wide average temperature increases with time due to moist convection. However, as these simulations are only 5 days long and the outer domain is quite large, the average temperature increase over the entire domain is 0.3 K.

The simulations are initialized with a weak, tropical-storm-like vortex with peak surface wind speed of 15 m s^{-1} in the eastern half of the outer domain. Given the highly idealized conditions, these vortices quickly grow into category 3, 4, or 5 TCs in approximately 96 hr, as shown in Figure 1. As noted above, simulation GS0.5 was produced differently, as it was too computationally expensive to simulate for 5 days. Rather, it was created by "spawning" an additional nested grid, using the commonly used 3:1 ratio, from GS1.5 at $t = 93$ hr. This allowed three hours for the convection and inner-core dynamics to adjust to the new resolution. The model fields were saved every one hour for the entirety of each simulation. From $t = 96$ to 108 hr the data from the innermost grid were saved every 2 min.

The sizes and intensities of the simulations during the high-frequency output period are also shown in Figure 1. Not surprisingly, the radii of maximum winds (RMWs) decrease and the peak surface wind speeds increase substantially as the inner grid spacing is changed from 2.0 to 0.5 km. The peak instantaneous wind speeds for GS0.5 are very high, occasionally exceeding 90 m s^{-1}. However, this is not indicative of an "extreme" level of category 5 intensity. Previous modeling studies have shown that as grid spacings decrease below 2 km, instantaneous wind speeds become representative of wind speeds sustained over periods of less than 1 min (Nolan et al., 2014; Rotunno et al., 2009) and should be corrected downward to define TC intensity. While such a correction is beyond the scope of this paper, we will note that the time-averaged values of the azimuthal-mean tangential winds at $z = 2$ km, which is a more stable and robust indicator of TC intensity, are 56, 60, 67, and 68 m s^{-1} for GS2.0, GS1.5, GS1.0, and GS0.5, respectively.

For a visual comparison of the TC structures, Figures 2 and 3 show snapshots at $t = 102$ hr of the simulated reflectivity in the inner core (within 100 km of the center), and the vertical velocity (w) over larger areas (within 280 km of the center) at $z = 2.8$ km (approximately flight level for most aircraft reconnaissance missions). The black contours on the reflectivity plots show $w > 3$ m s^{-1}, and the gray contours on the w plots show total condensate (cloud and rain) >4 g kg^{-1}. Although more details and smaller-scale structures are clearly evident for increasing resolution, the reflectivity fields are quite similar across the cases. The color scales on the w plots

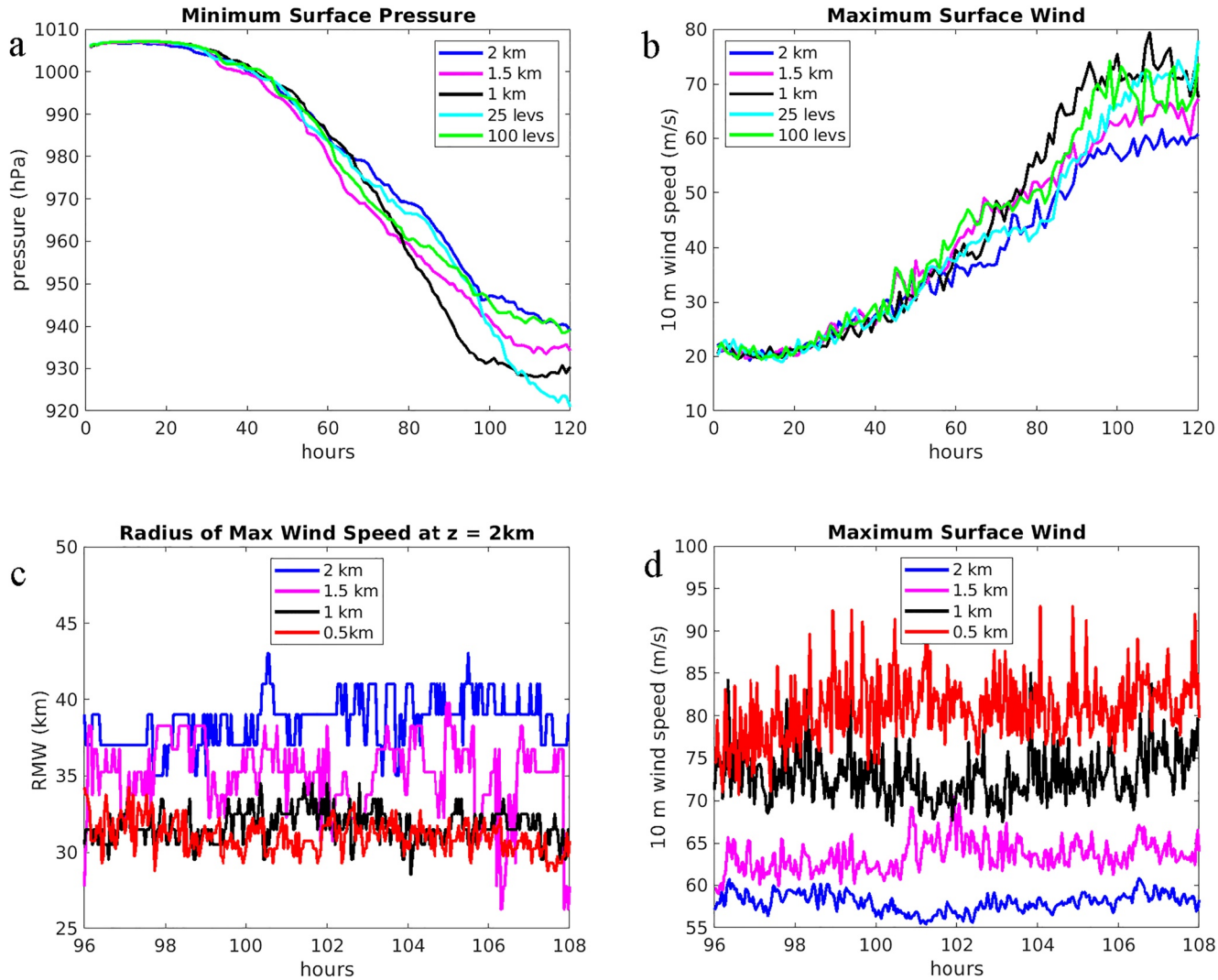

Figure 1. Intensities and sizes of the simulated TCs: (a) minimum surface pressure every 1 hr; (b) maximum surface wind speed; (c) radius of maximum azimuthal-mean tangential wind every 2 min during the high-frequency output period; (d) maximum surface wind speed every 2 min.

are restricted to ± 0.5 m s^{-1}, so that the gravity waves radiating outward into the far-field can be seen. As the grid spacing decreases, finer and finer scales are evident in the radiating waves. However, low-wavenumber spiral arms with radial widths of 10–20 km are apparent in all four simulations. In GS1.0 and GS0.5, these broader waves have higher frequency waves embedded within them. An animation of the w motions for GS1.0 is provided as Movie S1. Note that captions for this and subsequent movies can be found in Supporting Information S1.

The gray contours in Figure 3 indicate where active convection and precipitation are occurring. (Note that the eyewalls appear empty because only the 4 g kg^{-1} contour is plotted and much larger values are occurring there). All four simulations show regions of active rainbands 50–200 km from the TC centers. Below, we will attempt to distinguish the local vertical motions caused by rainbands from the gravity waves propagating outward from the eyewall.

3. Analysis Methods

3.1. Re-Mapping to Polar Coordinates

Most of the results that follow are based on a remapping of the model output on specified model levels into polar coordinates. Although the WRF vertical coordinate is not based on height, but rather on the hydrostatic pressure

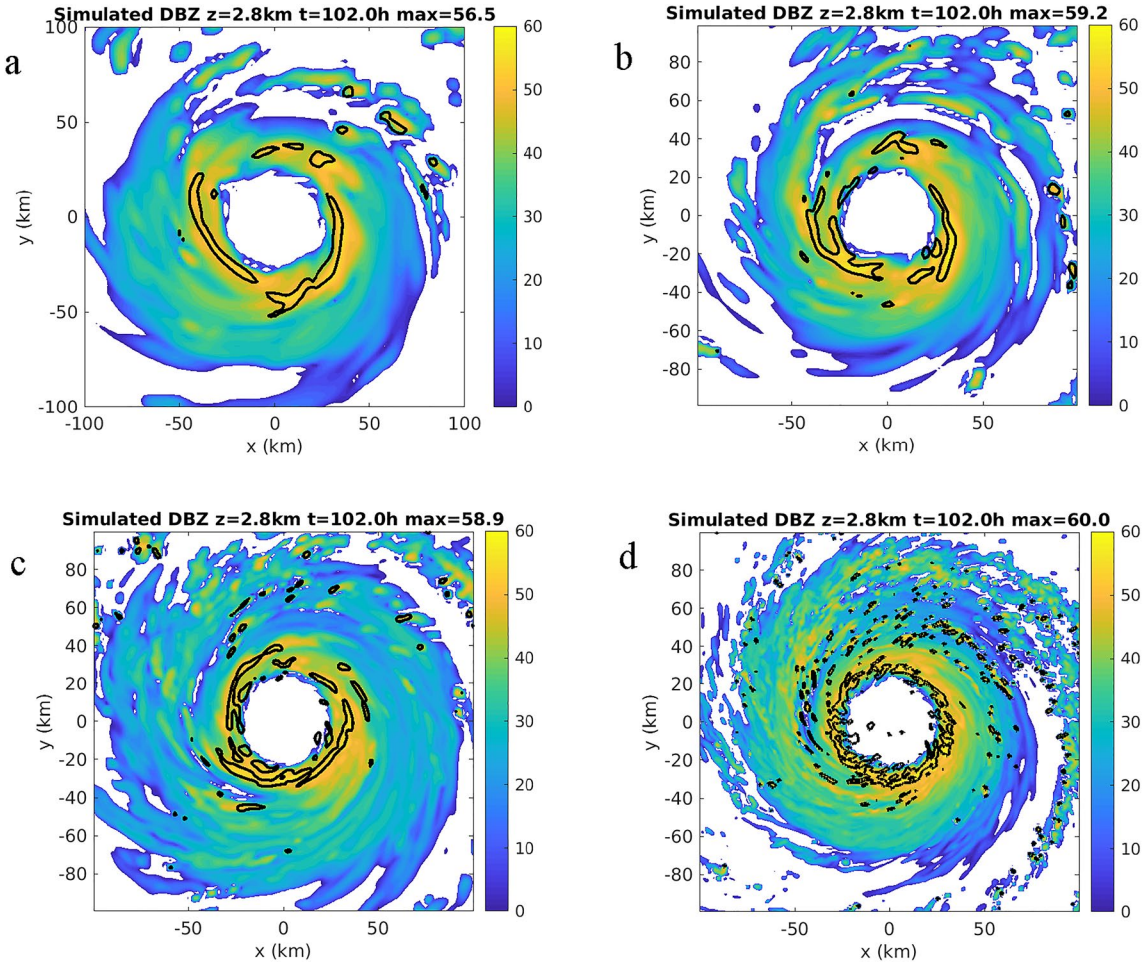

Figure 2. Simulated reflectivity images for (a) GS2.0; (b) GS1.5; (c) GS1.0; (d) GS0.5. Black contours indicate vertical velocities exceeding 2 ms^{-1}.

of the dry air mass, the model levels tend to be quite constant in height across the domain. For example, the plots in Figures 2 and 3 are generated from model level 15. The altitudes of the model points in the plot for GS1.0 range from 2.78 to 2.84 km with a mean value of 2.80 km.

With their high intensities and very low environmental wind shears, these TCs have almost no vertical tilt. The TC centers are defined by the centroid of the negative of the surface pressure anomaly in a 200 × 200 km box similar to Nguyen et al. (2014): after placing a box on a first guess that is the center of the inner nest, the centroid of pressure anomaly is used as the center of the next box, and the process is repeated three times to produce a final center.

The data on Cartesian grids are bilinearly interpolated onto a polar grid with radial grid points at $r = \Delta x$, $2\Delta x$, … to $r = 300$ km, except for GS0.5, where the outer point is at $r = 280$ km. At each radius there are 512 points in the azimuthal direction. This is of course grossly over-sampled at small radius, but the data become under-sampled azimuthally at $r = 244$ km, $r = 162$ km, and $r = 81$ km for GS1.5, GS1.0, and GS0.5. Nonetheless, the SGWs are accurately represented in the remapped fields, even at large radius.

3.2. Spectral Filtering

The purpose of spectral filtering is to remove or reduce most of the vertical motions or surface anomalies associated with moist convective updrafts in the rainbands. The prevailing locations and time evolution of these updrafts can be seen in Figure 4a, which shows a time-radius Hovmöller diagram for the vertical velocities along the direction emanating due northeast of the center of the TC in GS1.0. The active rainband regions are identified

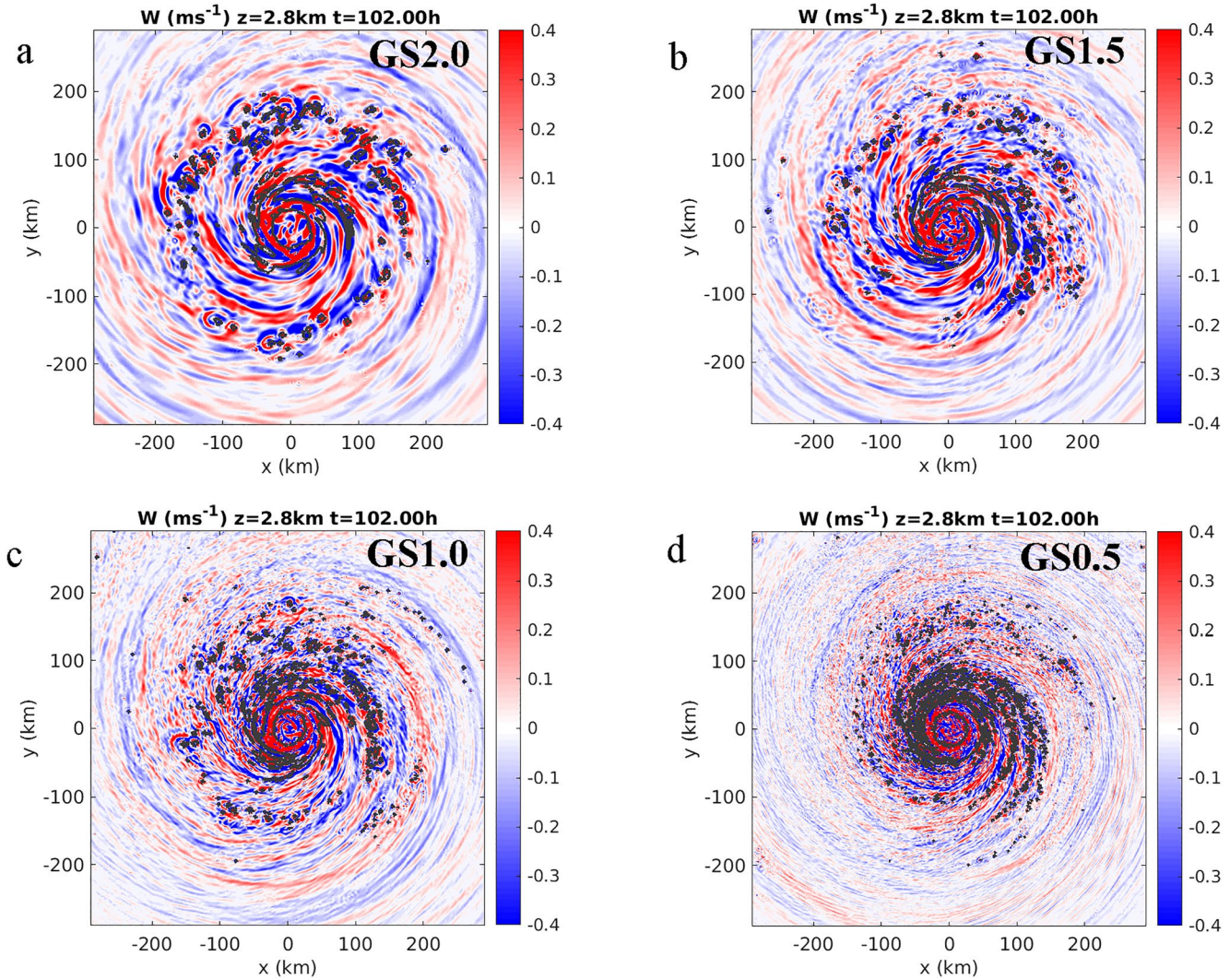

Figure 3. Vertical velocity (w) at $t = 102$ hr for (a) GS2.0; (b) GS1.5; (c) GS1.0; (d) GS0.5. Dark gray contours indicate total condensate exceeding 5 g kg^{-1}.

by the localized clusters of upward and downward motions (red and blue colors) between $r = 100$ and 200 km; in addition, the black contours show $w > 2$ m s^{-1}. Even before filtering, the outward propagation of gravity waves is evident by the bands of oscillating anomalies that extend upward and to the right from $r = 150$ to 300 km, which we will refer to as the "radiation region".

The gravity waves propagate outward and have substantial power in low azimuthal wavenumbers, that is, the fairly thick spirals that can be seen in Figure 3. The convective cells do not propagate outward, and they have short scales (wavelengths) in the azimuthal direction. In addition, from the point of view of a fixed location, a convective updraft has a short time period (high frequency) in the temporal direction as it is carried along rapidly by the tangential wind. Since their phase lines are wrapped in spirals, even the gravity waves with fairly short radial wavelengths appear to have lower frequencies from the perspective of a fixed point in (r, λ). We first perform a band-pass filtering in time at each grid point in (r, λ), allowing motions with periods τ ranging from, for example, 360–3,600 s. Then, at each time and radius, the data is low-pass filtered in the azimuthal direction, keeping all power in some range of azimuthal wavenumbers, such as $n = 2$ to $n = 64$.

An example is shown in Figure 4b, which is the result of filtering the data in Figure 4a for the aforementioned periods and wavenumbers. While the w field is still fairly noisy, the trajectories of the high-frequency waves in w are more apparent, and many of the convective cells have been diminished or nearly eliminated. This helps to isolate

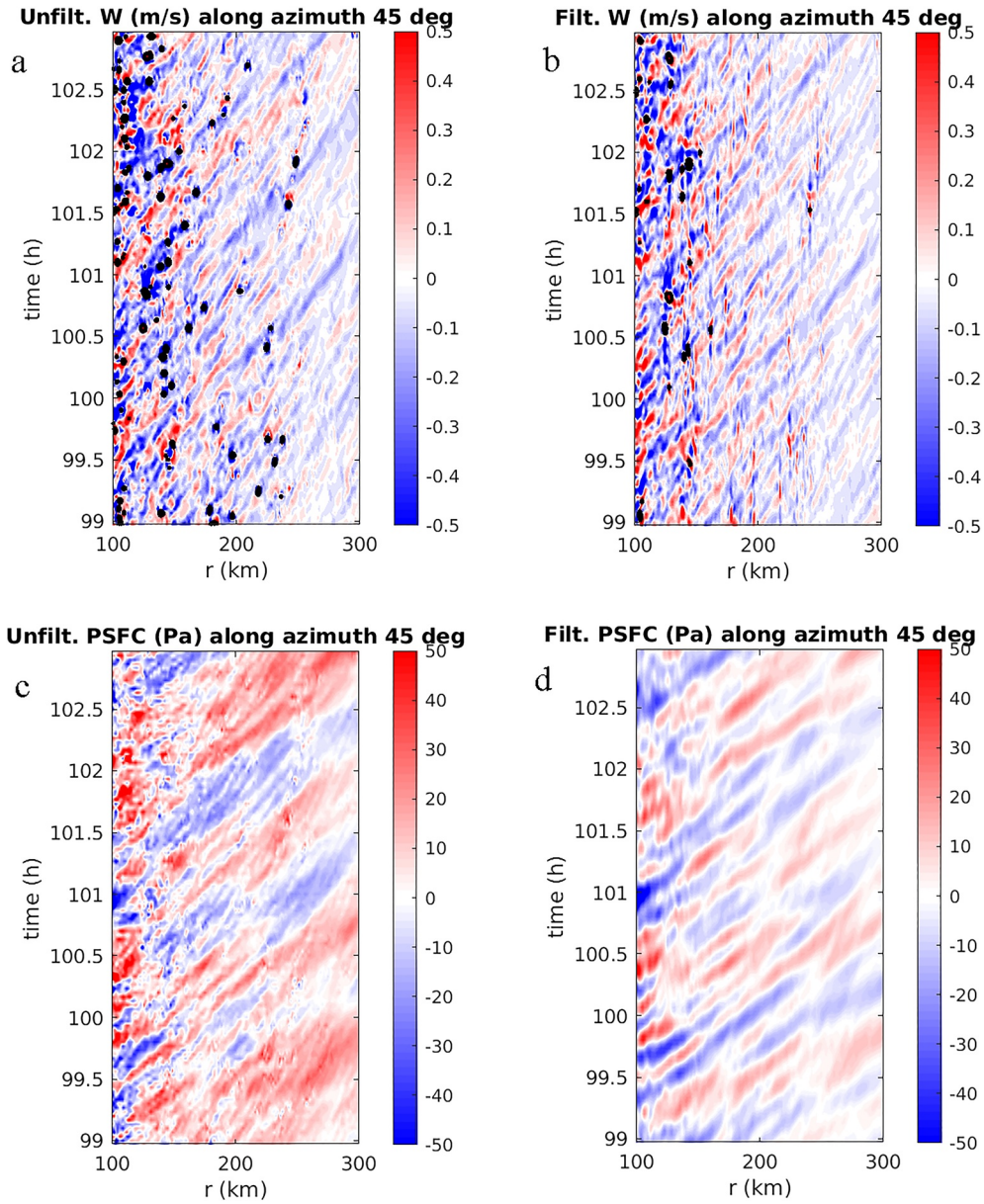

Figure 4. Radius-time Hovmöller diagrams for w and p at $z = 2.8$ km in GS1.0, along a ray emanating at $\lambda = 45°$ from the TC centers: (a) unfiltered w; (b) w after FILT-W is applied; (c) unfiltered p; (d) p after FILT-P is applied. Black contours indicate w >2 m s^{-1}.

the radial wavelength and radial phase speed of the spiral waves. The bandpass filtering with 360 s $\leq \tau \leq$ 3,600 s and $2 \leq n \leq 64$ is hereafter referred to as FILT-W (see Table 2).

Table 2
Properties of the Filters

Filter name	Azimuthal wavenumbers	Time scales (s)
FILT-W	$2 \leq n \leq 64$	$360 \leq t \leq 3{,}600$
FILT-P	$2 \leq n \leq 16$	$720 \leq t \leq 7{,}200$
FILT-S	$2 \leq n \leq 64$	$360 \leq t \leq 7{,}200$
FILT-B	$2 \leq n \leq 256$	$240 \leq t \leq 21600$

As noted in NZ17 and N20, the surface pressure (hereafter p_s) signals associated with SGWs tend to be of lower wavenumbers and longer radial wavelengths. This is evident in the unfiltered data shown in Figure 4c, where oscillations with period around 1 hr can easily be seen beyond $r = 200$ km. (While we say "unfiltered," the azimuthal mean value of surface pressure at each radius is removed before making the plot; otherwise we would only see the very large radial variation of pressure). To enhance these waves, bandpass filtering is applied for 720 s $\leq t \leq$ 7,200 s and $2 \leq t \leq 16$, hereafter FILT-P. The result shown in Figure 4d has almost no sign of the convective cells.

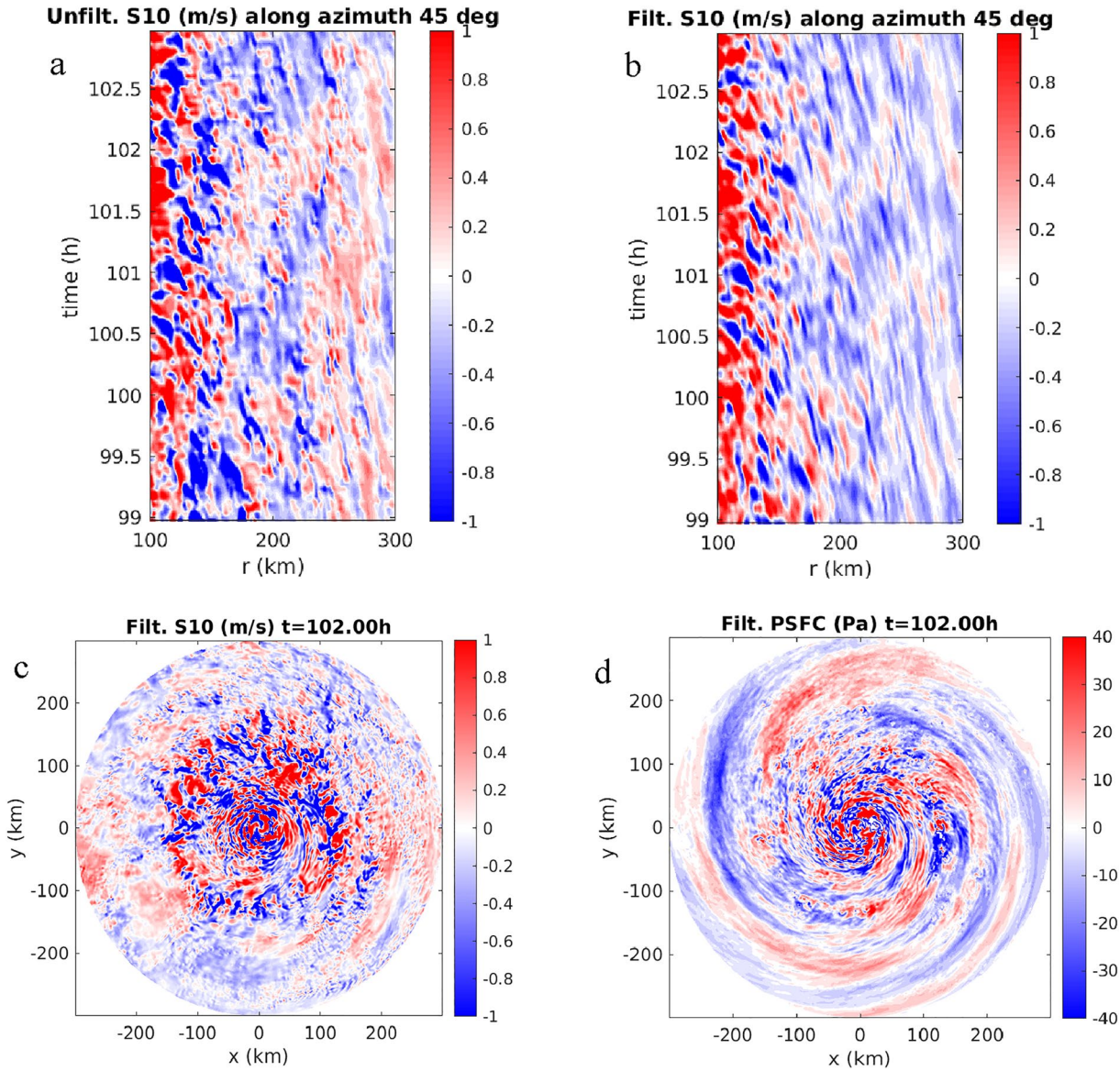

Figure 5. Surface wind speed (S10) and surface pressure in GS1.0: (a) unfiltered S10 along $\lambda = 45°$; (b) S10 with FILT-S; (c) surface field of S10 with FILT-S; (d) surface pressure with FILT-B.

A Hovmöller diagram for the unfiltered (azimuthal mean removed) 10-m wind speed (hereafter S10) is shown in Figure 5a. The result is surprising in that only a hint of outward propagation can be seen, and in fact the predominant motion for the S10 anomalies is inward. Since it is not clear whether to bandpass "high" or "low" for S10, Figure 5b shows the same data bandpassed with the even broader ranges of 360 s $\leq t \leq$ 7,200 s and $2 \leq n \leq 64$ (FILT-S). Still, only inward propagation can be seen. In the other quadrants, any apparent inward or outward motion of S10 anomalies was even less clear (not shown). For a more comprehensive view of the anomalous S10 field, the filtered data can be projected back onto the Cartesian grid, as shown in Figure 5c. To see even more detail, the bandpass windows are widened further to 240 s $\leq t \leq$ 21,600 s and $2 \leq n \leq 256$ (i.e., nearly no filtering at all, this is FILT-B). Along with $n = 0$, $n = 1$ must be removed, otherwise S10 only shows the very large $n = 1$ pattern caused by the storm motion. Along with the absence of inward propagation, it is surprising that the S10 field shows only marginal signs of streamwise rolls or streaks that are widely observed in TCs (Gall et al., 1998; Morrison et al., 2005; Nolan, 2005), and only near the inner core. While some wind streaks roughly aligned with the low-level flow are visible for $r < 100$ km, these are non-existent for $r > 200$ km. In contrast, the minimally

filtered ps field shown in Figure 5d clearly shows low-frequency radiating bands, as expected from NZ17 and N20. An animation of Figure 5d is provided in Movie S2.

3.3. Power Spectra in the Radial Direction

To estimate the predominant wavelength in the radial direction, power spectra are computed using Fourier transforms in the radial direction. Unlike the azimuthal direction, which is periodic, or the time direction, for which the unsteady fields are reasonably close to a steady-state, the data are neither periodic nor steady in the radial direction. Nonetheless, as is evident from the Hovmöller figures above, the outward moving waves do appear approximately steady in the GW radiation region. To serve both the purpose of improving the quality of the power spectrum and to eliminate the data from the eyewall region (which cannot be mitigated by filtering), a windowing function is applied to the data before each transform is applied in the radial direction. The function is the standard Welch window recommended by Press et al. (1992), except that instead of going to zero at both ends of the interval (e.g., $r = 0$ and $r = 300$ km), it goes to zero at $r = 80$ km such that the data inside that radius is zeroed out. Thus, in addition to the effects of the filtering, vertical motions in and around the eyewall are not considered in the estimates of radial wavelength.

4. Results

4.1. Radial Length Scales

We seek to determine the predominant radial wavelengths of the radiating waves, how these change with grid spacing, and whether the observed values can be matched.

The aircraft observations of w inside TCs, as presented in NZ17, were taken at pressure altitudes ranging from 850 to 700 hPa. We focus on w near 700 hPa, as the majority of NOAA P3 aircraft penetrations occur at this altitude (Aberson et al., 2006). Model level 15, shown in the figures above, is closest to this level. After remapping and filtering, data are taken along rays of constant azimuthal angle distributed evenly around the TC. Using the windowing function described above, Fourier series and power spectra are computed for each radial vector of data. To reduce oversampling, samples are taken every four points (out of 512) in the azimuthal direction and every four steps in time (8 min). The final result is the average over these 11,520 power spectra.

Figure 6 shows the power spectra density (PSD) multiplied by wavenumber to produce so-called "variance preserving" PSD plots. First, Figure 6a shows the results for w in GS2.0, GS1.5, GS1.0, and GS0.5 without the azimuthal and temporal filtering. The radial wavelengths with peak power are 16.7, 13.0, 7.7, and 4.9 km, respectively. The maximum power and its integral (the total variance) in w decrease somewhat as the resolution changes from GS2.0 to GS1.0, but then increase again for GS0.5. However, without filtering, we know that a considerable part of the "power" in w comes from the small-scale convective updrafts, as can be seen in Figures 3 and 4. Figure 6b shows the radial PSDs after filtering for the higher-frequency gravity waves using FILT-W. After filtering, the peak wavelengths are shifted to 18.8, 13.6, 9.5, and 6.7 km, and the power in w decreases with decreasing grid spacing. This could be due to several factors, such as the increasingly nonhydrostatic dynamics of the increasingly smaller updrafts (Morrison, 2016) and more rapid dissipation of smaller-scale waves due to both physical and numerical dissipation in the model (Skamarock, 2004). Unfortunately, it appears that the peak radial wavelength for the w waves does not "converge" as the grid spacing decreases from 2.0 to 0.5 km, but simply continues to decrease with Δx. On the other hand, peak wavelengths for both GS1.0 and GS0.5 are not far off from the range of predominant wavelengths observed by NZ17, which was 4–8 km.

Radial power spectra are also computed for surface pressure. If no filtering is applied to the surface pressure field, then even the variance-preserving PSD will have its greatest power in the largest scale (the curve will peak at the right edge). This is because the surface pressure field has a large amplitude $n = 1$ asymmetry that also varies very slowly with radius, that is, at each azimuth it is either positive or negative from the TC center out to 300 km and beyond. Since the PSD calculation takes the square of the Fourier coefficients, they don't cancel out when averaged around the azimuth. Therefore, as an equivalent to the "unfiltered" result shown for w, Figure 6c shows the radial PSDs after applying FILT-B. For GS2.0 and GS1.5, the peak wavelength is 100 km, and both show secondary peaks at 50 km. For GS1.0, the peaks are at 75 and 43 km, but the PSD is fairly flat. For GS0.5, the peak is at 70 km, but the nearby secondary peak is not present. Rather, there is another broad peak at smaller

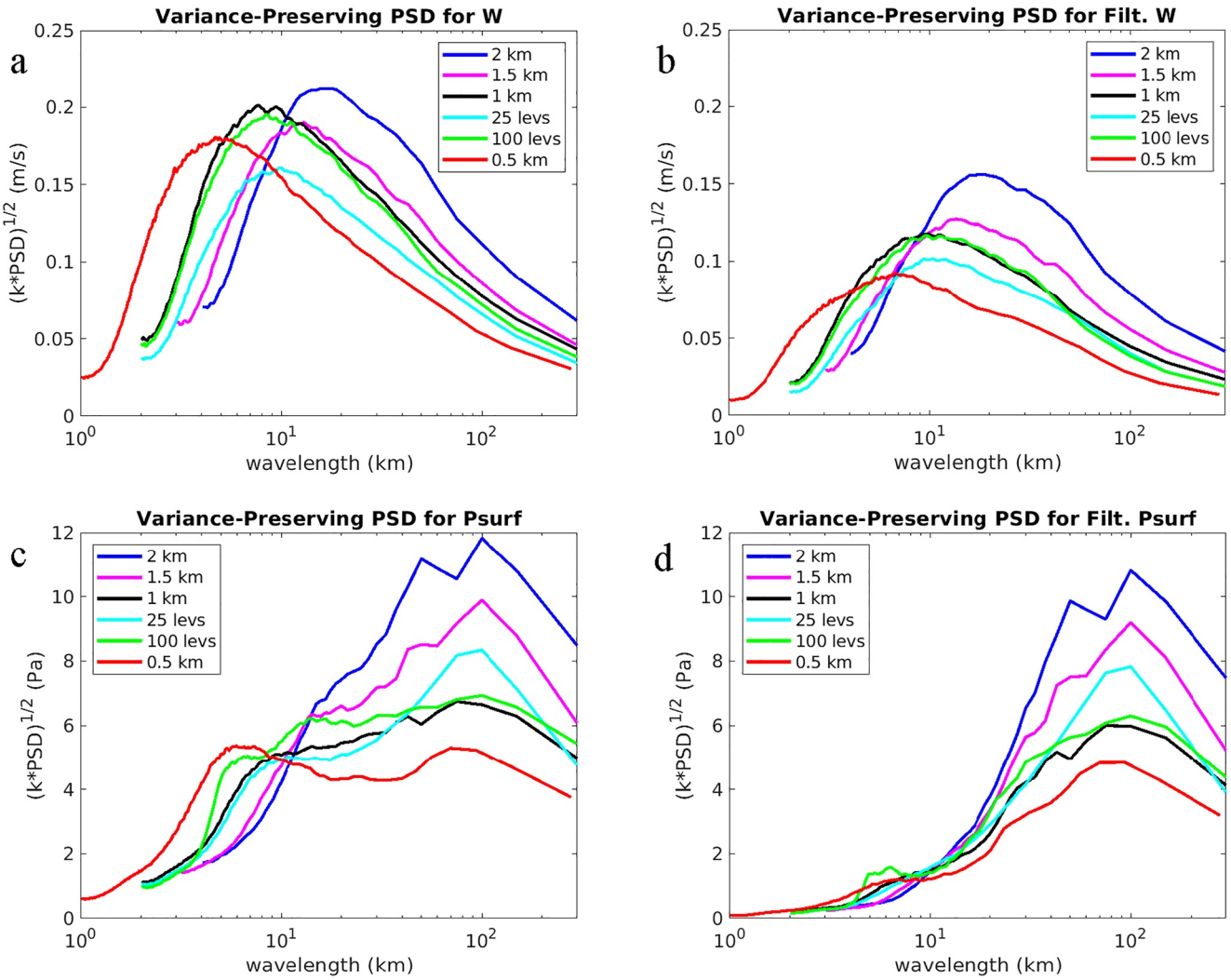

Figure 6. Variance-preserving power spectra along radial samples of data from the simulations: (a) PSDs for w without filtering; (b) for w with FILT-W; (c) for p with FILT-B; (d) for p with FILT-P.

scales from 5 to 8 km. Without further spatial and temporal filtering, the PSD reveals a strong signal from surface pressure anomalies under and around convective updrafts in the rainband region.

In contrast, Figure 6d shows the PSDs after FILT-P is applied. All the aforementioned long-wavelength spectral peaks are retained (although slightly decreased in amplitude), while the power in small scales has been almost eliminated. The peak power (and thus amplitude) of the low-frequency p waves decreases considerably as grid spacing decreases. However, the peak wavelength decreases only from 100 km for GS2.0 to 70 km for GS0.5. The difference between GS1.0 and GS0.5 is quite small, suggesting that the p waves are becoming well resolved for grid spacings of 1.0 km and less.

4.2. Phase Speeds

As for wavelength, we seek to systematically measure the radial propagation speeds of the SGWs. Subjective analyses of the radius-time Hovmöller plots can find phase speeds for w waves ranging from 20 to 30 m s^{-1}, and 50 to 80 m s^{-1} for pressure waves, which are consistent with the findings in NZ17 and N21.

For a more objective analysis we use the following procedure. First, lines in (r, t) space are defined by common starting and ending points in radius, r_s and r_e, and a series of starting points in time, t_1, t_2, etc. For each starting point in time, a vector of points in (r, t) are defined by regular intervals in r (Δr) and in time (Δt), where

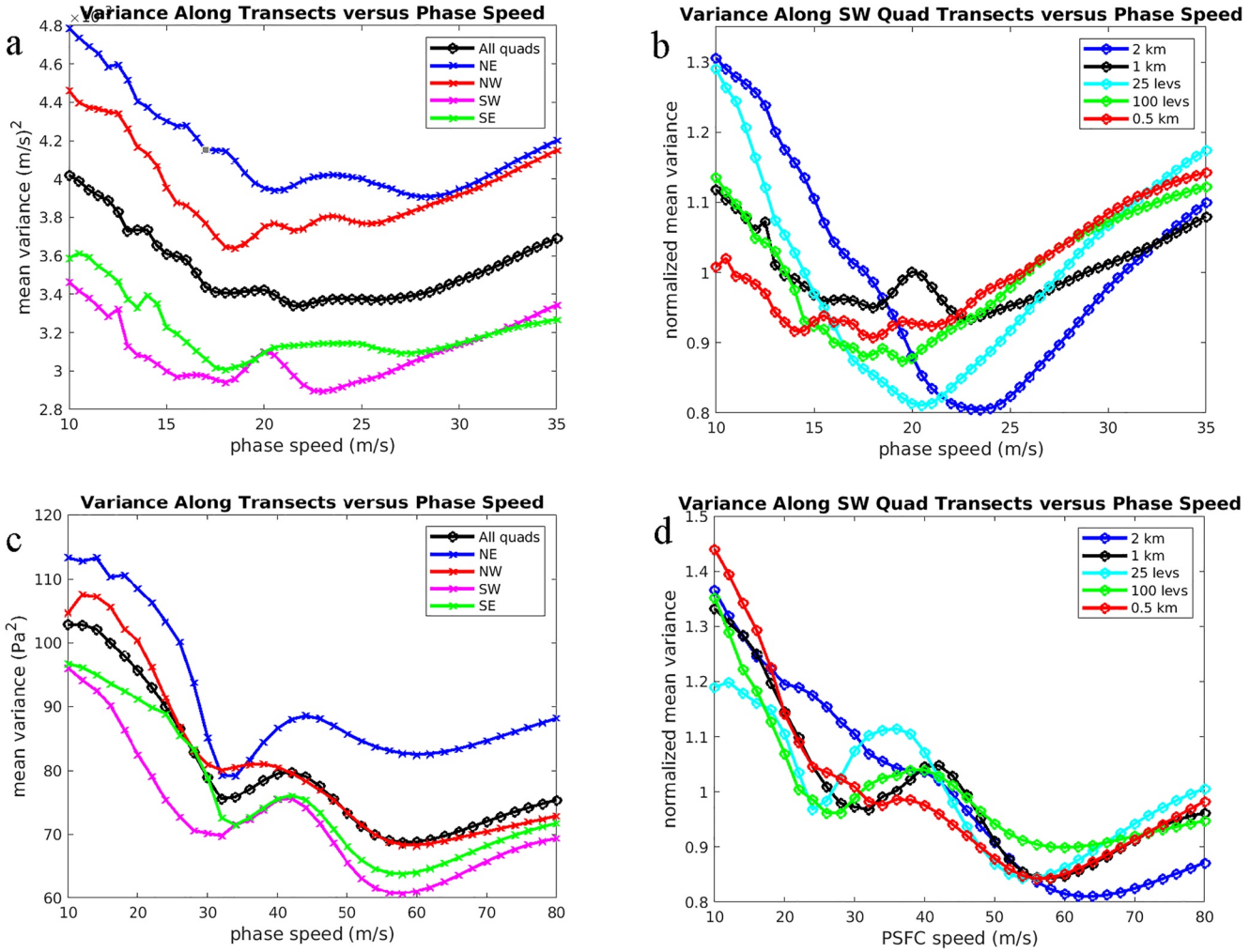

Figure 7. Indications of predominant phase speeds of the waves by mean variance along lines in (r, t) space as a function of phase speed: (a) for w with FILT-W in GS1.0; (b) for w with FILT-W in most of the all simulations, SW quadrant only; (c) for p with FILT-P in GS1.0; (c) for p with FILT-P in most of the all simulations, SW quadrant.

$\Delta t = \Delta r/c_p$, and c_p is a constant phase speed. For each azimuth angle (e.g., a data set that looks like the Hovmöller diagrams), the data is interpolated to these outward propagating lines of constant phase speed. Our premise is that the mean variance of the w or p data along these lines will be minimized for the speed that best corresponds to the dominant SGWs.

Focusing on w waves in the SGW radiation region, we use $r_s = 200$ km and $r_e = 280$ km. The start times are from $t_1 = 1.0$ hr to $t_{41} = 9.0$ hr with 0.2 hr intervals. Data are interpolated to these rays starting at these times and along 32 different azimuth angles from $\lambda = 0°$ to $\lambda = 354.75°$ (11.25° spacings). The mean variance along the rays of each phase speed are shown in Figure 7a. The black curve shows the result for rays in all quadrants of GS1.0. There is a minimum in variance for $c_p = 22$ m s^{-1}, and the curve suggests that there may be other preferred speeds at 17 and 27 m s^{-1}. Although there is a clear minimum at 22 m s^{-1}, the change in variance across the range of c_p from 10 to 35 m s^{-1} is not as large, nor are the minima as clear, as we might have hoped. Revisiting Figure 4a, we can see that even along the most obvious phase lines of the SGWs, there is a lot of variability and residual noise.

The black curve shows the result averaged over all quadrants, but we can see from the other curves that the predominant speeds are more distinct in each quadrant. The NE quadrant has distinct minima at 20 and 28 m s^{-1}, NW has minima at 18, 22, and 26 m s^{-1}, SW at 18 and 23 m s^{-1}, and SE has minima at 18 and 27 m s^{-1}. The variations around the different quadrants explains why the results for all quadrants (black curve) are less distinct. These differences in GW properties by quadrant are consistent with the findings of N20 using the linear model:

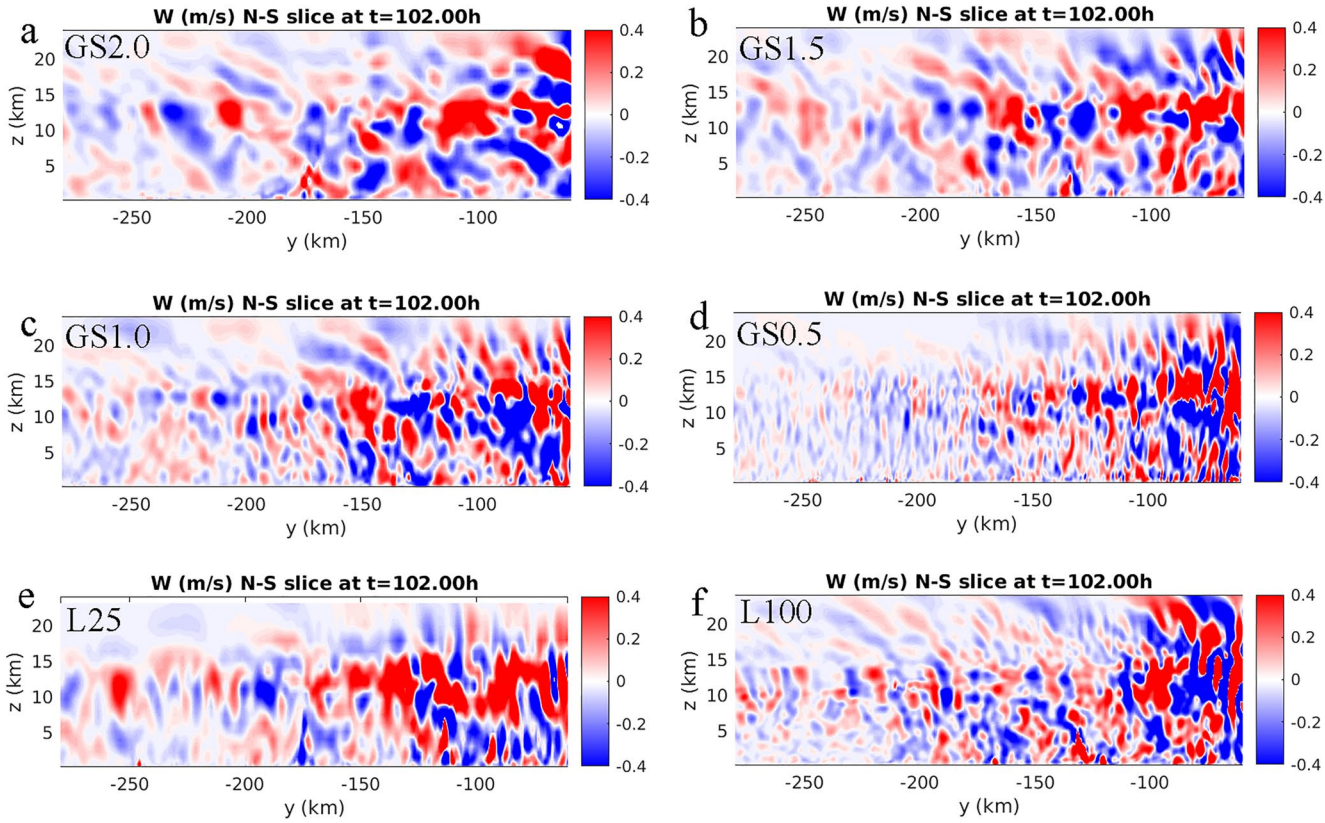

Figure 8. South to north vertical slices of w in (a) GS2.0; (b) GS1.5; (c) GS1.0; (d) GS0.5; (e) L25; (f) L100. The plots show data from 280 to 60 km south of the TC centers.

convective pulsing in the preferred convection region of the eyewall, usually the downshear left quadrant, projects onto waves of different vertical and horizontal structures with different phase speeds. Furthermore, outside the eyewall the waves are also rapidly advected azimuthally by the tangential flow. The waves with faster radial propagation "escape" from the core sooner, while slower waves may be carried into the next quadrant before they travel outward into the SGW radiation region. Examples of these behaviors are shown in Figures 4 and 8 of N20.

Observationally, the only measurements of outward phase speed that we have for flight-level w waves is the 22 m s^{-1} estimate from NZ17, which was computed from the difference in the apparent wavelengths measured by inbound and outbound aircraft, and averaged over many different flights and different TCs. Most of the phase speeds above are consistent with this observational estimate.

Figure 7b shows the variance as a function of phase speed for simulations GS2.0, GS1.0, and GS0.5, using data from the SW quadrant of each case, as this quadrant has the most pronounced minima. Each curve has been normalized by its mean value. GS2.0 shows a single predominant c_p of 23 m s^{-1}. For GS1.0 and GS0.5, the phase speeds are slightly less, and additional phase speeds are evident around 18 and 15 m s^{-1}. The higher resolution in these two simulations permits better representation of finer-scale waves which propagate more slowly, as suggested by the classic gravity wave dispersion relation and shown in N20. The results for L25 and L100 will be discussed below.

Currently there is no observational estimate for the outward phase speed of the surface pressure waves, and the only value for comparisons is the 70 m s^{-1} estimate in N20 from the linear model and from the dispersion relation. The same procedure above was used to identify the predominant phase speeds for the surface pressure, except that the rays are defined from $r = 100$ to 280 km to account for the longer radial wavelengths and faster speeds of the pressure waves. As shown in Figure 7c, all quadrants show minima in variance in two ranges of c_p: from 20 to 30 ms^{-1} and from 55 to 65 m s^{-1}. The faster phase speeds are associated with the "fast" pressure waves discussed in N20 that are also visible in Figure 4. This analysis reveals that a second class of p waves are present, which

may be associated with a surface signature of the predominant w waves which have c_p in the 15–30 m s^{-1} range (Figure 7a, extended to higher c_p, does not show additional minima). Looking more closely at Figure 4d, we can see evidence of bands of propagation at slower speeds and with shorter radial scales. These shorter waves may be the reason for the "shoulders" of the PSDs apparent in Figure 6d.

Figure 7d shows how c_p values for the p waves change with increasing resolution. For GS2.0, the p waves are the fastest, around 65 m s^{-1}, with only a hint of the secondary c_p around 35 m s^{-1}. GS1.0 shows distinct peaks at 58 and 31 m s^{-1}, and the values for GS0.5 are nearly the same.

4.3. Changes With Vertical Resolution

Additional simulations using 1 km grid spacing were performed with half and twice as many vertical levels (L25 and L100). Horizontal slices of w, filtered w and filtered p, and Hovmöller diagrams were very similar to those of GS1.0 (not shown). As shown in Figure 6, the PSDs for L100 are nearly identical to GS1.0. For L25, the PSD for w has less power and the PSD for p has more power, but the peak values for each are nearly identical to GS1.0 and L100.

For phase speeds of w waves, L25 is more similar to GS2.0 than to GS1.0 or GS0.5, having a single predominant value, although at a slower speed (21 vs. 24 m s^{-1}). On the other hand, for p waves, L25 is similar to GS1.0, showing two distinct minima in variance for fast and slow waves. L100 is also similar to the others for p waves, but for the w waves, it only indicates c_p values less than 20 m s^{-1}, without an additional signal around 23 m s^{-1}, as for GS1.0 and GS0.5. However, for other quadrants, the L100 curve was more similar to the others (not shown).

All the simulations show somewhat different values for the predominant radial wavelengths and phase speeds for w and p waves. As either horizontal or vertical resolution increases, the diversity of waves increases. For example, GS2.0 shows only one distinct phase speed in both w and p, while L25 shows only one phase speed in w. All the other simulations have signs of multiple phase speeds in w and p. While some of these differences may be due to resolution, part of the differences may also exist because the simulated TCs themselves are each of slightly different sizes and intensities. This leads not only to differences in wave energy, but also to differences in which quadrant the waves are predominant, relative to their generation source in the downshear left quadrant. It is beyond the scope of this paper to sort out these nuances for each type of wave in each quadrant. We can conclude that, in these simulations, the radial wavelengths and phase speeds of the SGWs are generally consistent with observations and with each other. We can also conclude that, unfortunately, except for the radial wavelength of the p waves, these properties continue to change as the grid spacing decreases, and we cannot say with confidence that the solutions are converging. The grid spacing may need to decrease further, perhaps to 0.25 km, before the observed wavelengths of 4–6 km can be resolved.

4.4. Vertical Structure

For a first look at the vertical structure of the radiating waves, Figure 8 shows snapshots of vertical slices of w in the y-z plane in the region from 60 to 280 km south of the center of each simulated TC. In all six plots there appear to be many overlapping waves of different vertical and radial scales. An animation for GS1.0 is provided as Movie S3. The w anomalies propagate outward, with some coherence over short time scales, but the SGWs are generally more difficult to identify as compared to what can be seen in the horizontal slices shown above. All the plots show the strongest vertical motions occurring in the upper troposphere, embedded in the upper-level outflow. The radial scales of the w anomalies decrease as the grid spacing decreases from 2.0 km down to 0.5 km, and the vertical scales also decrease, but not to the same degree. Figures 8e and 8f show w for L25 and L100. The vertical scales for L25 are clearly larger than for GS1.0, while they are only slightly smaller for L100. An interesting feature of L100 is the much more sharply defined change in the w field along the tropopause around $z = 14$ km.

To quantitatively diagnose the vertical structure of the SGWs, NZ17 used the following procedure. At a designated point moving with the TC, a column of w data at each vertical level is extracted from the 3D fields and interpolated to a regularly spaced grid in the vertical direction with $\Delta z = 250$ m. Time series of these columns are recorded, making a data set of $w(z,t)$. The correlation matrix of this data is constructed and used to compute

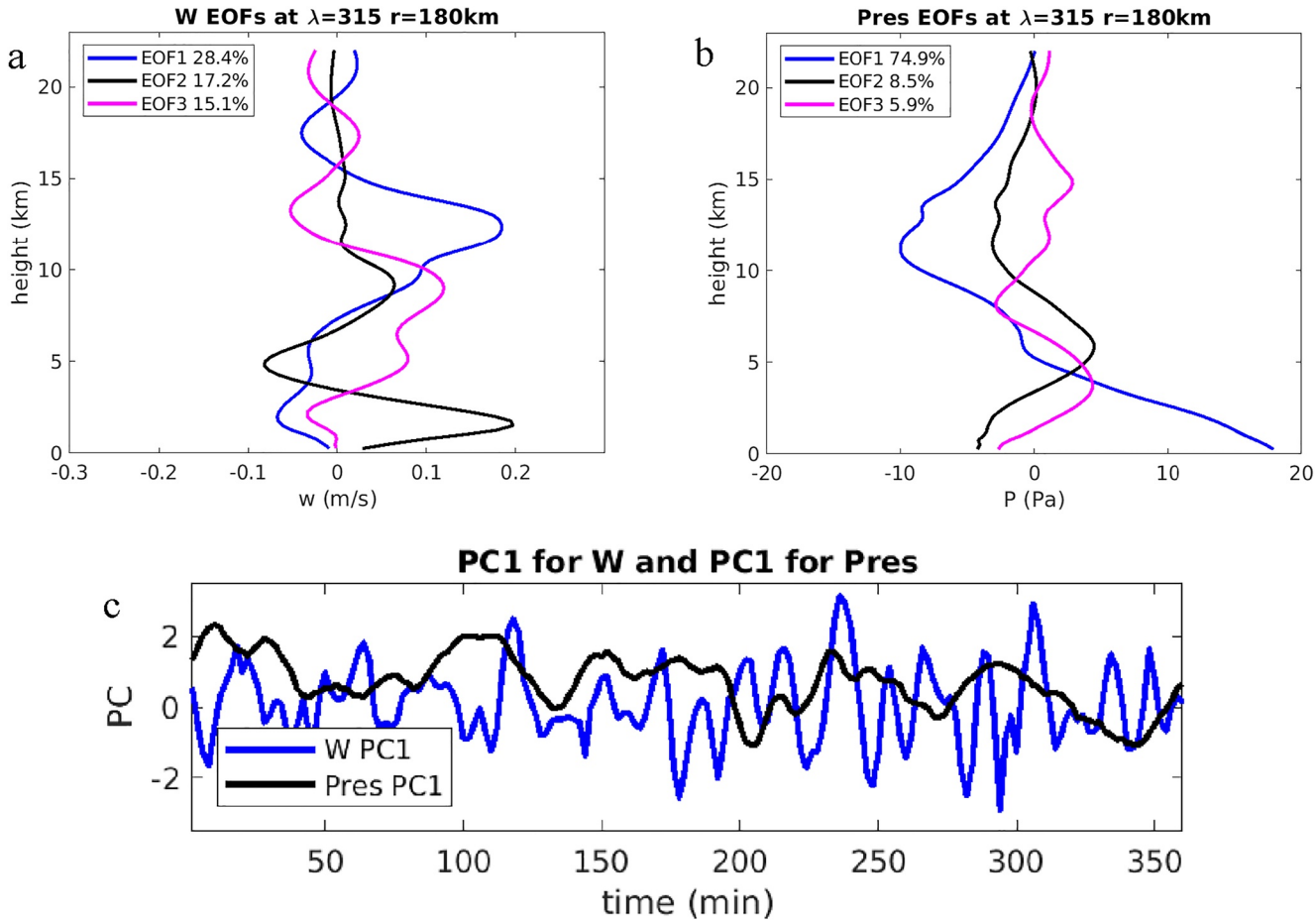

Figure 9. Empirical orthogonal functions (EOFs) of time-height data of *w* and *p* for GS1.0: (a) WEOFs; (b) PEOFs; (c) first principal components (PC1) for *w* and *p*.

empirical orthogonal functions (EOFs) of *w*. NZ17 found that, in most cases, the first two EOFs represented a deep wave of approximately the first baroclinic mode and a secondary wave with higher vertical wavenumber.

This procedure is repeated here with our new simulations, with the modification that the vertical columns of w are the average over the point of interest and its 8 nearest neighbors (a 3 × 3 grid of points). The data are taken from the unfiltered model output. We focus on the EOFs of *w* passing through a point 180 km SE of the center, that is, in the middle of the SE quadrant, where on average the least rainband activity occurs. In addition, we apply the same procedure to *p*.

Vertical profiles of the first three EOFs for *w* in GS1.0 are shown in Figure 9a. The first EOF (WEOF1) has a vertical wavenumber one structure in the troposphere and represents 28% of the variance. The second and third modes have their strongest motions in the middle and lower troposphere, with 17% and 15% of the variance, respectively. The principal component for WEOF1 (WPC1, i.e., the extent to which WEOF1 projects onto the *w* data at each point in time) is shown in the blue curve in Figure 9c, and we can see it oscillates with a period of about 20 min.

NZ17 attempted to relate the *w* waves to the *p* waves by computing the correlation between the *p* data and the WPCs. They found that WEOF1 was well correlated with a vertically varying pressure anomaly that had its strongest value at the surface. Their interpretation was that WEOF1 was the vertical motions associated with the larger-scale *p* wave. However, similar results could not be reproduced with these new simulations. Instead, we find that the EOFs for *w* and the EOFs for *p* are not dynamically coupled. Figure 9b shows the first three EOFs for p. EOF1 dominates with 75% of the variance, and it does have its maximum value at the surface. Its principal component (PPC1) is shown in the black curve in Figure 9c, and it clearly has a different period of about 80 min. It appears that the higher-frequency *w* waves and the lower-frequency *p* waves are entirely decoupled. There

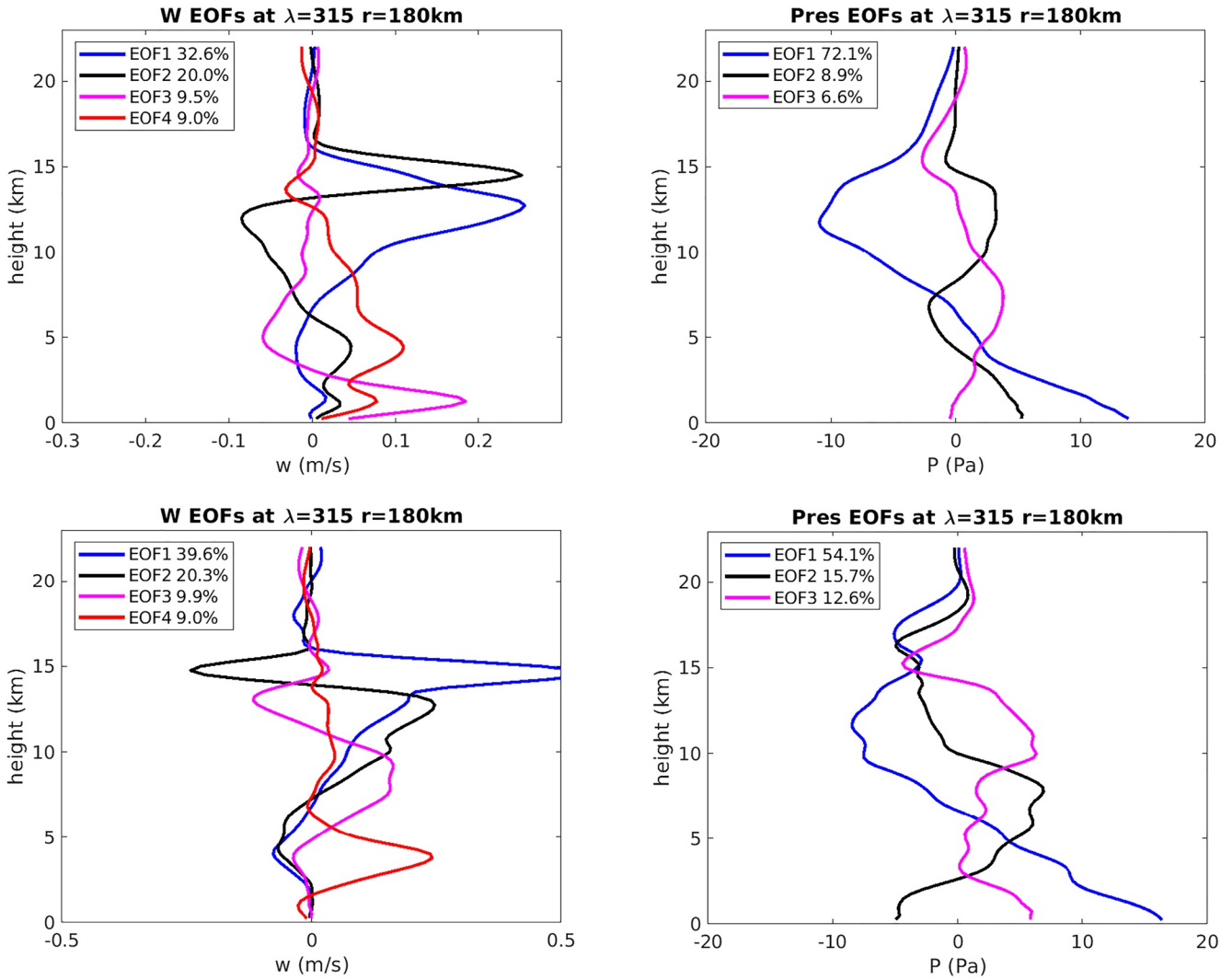

Figure 10. EOFs for the higher-resolution simulations: (a) WEOFs for GS0.5; (b) PEOFs for GS0.5; (c) WEOFs for L100; (d) PEOFs for L100.

should be some vertical motions associated with the pressure waves, but perhaps they are too small to be differentiated from the stronger motions of the numerous *w* waves.

The EOFs for simulations with lesser resolution, GS2.0, GS1.5, and L25, are very similar to those of GS1.0, although with smoother structures in the vertical direction (not shown). The WEOFs and PEOFs for simulations with increased resolution, GS0.5 and L100, are shown in Figure 10. For *w*, the first two EOFs are maximized in the upper troposphere, while the third and fourth EOFs are necessary to capture the motions in the middle and lower troposphere. The PEOFs are similar to those of GS1.0.

5. Spiral Gravity Waves in the Outflow

As noted in NZ17, there is visual evidence for outward propagating SGWs in the upper-level outflows of TCs. However, the interpretation of cloud motions or the propagation of any feature is complicated by the fact that there is strong outflow in the upper levels of a tropical cyclone, with outward radial velocities exceeding 15 m s^{-1}. Does this mean that the outflow speed is simply added to the phase speed? Or do the waves propagate at a constant speed with vertical coherence, as suggested by the EOF analyses above?

The left column of Figure 11 shows snapshots of *w* on model level 40 (mean altitude $z = 14.4$ km) for GS2.0, GS1.5, and GS1.0. Low-wavenumber spiral bands of *w* are evident, especially in the radiation region beyond

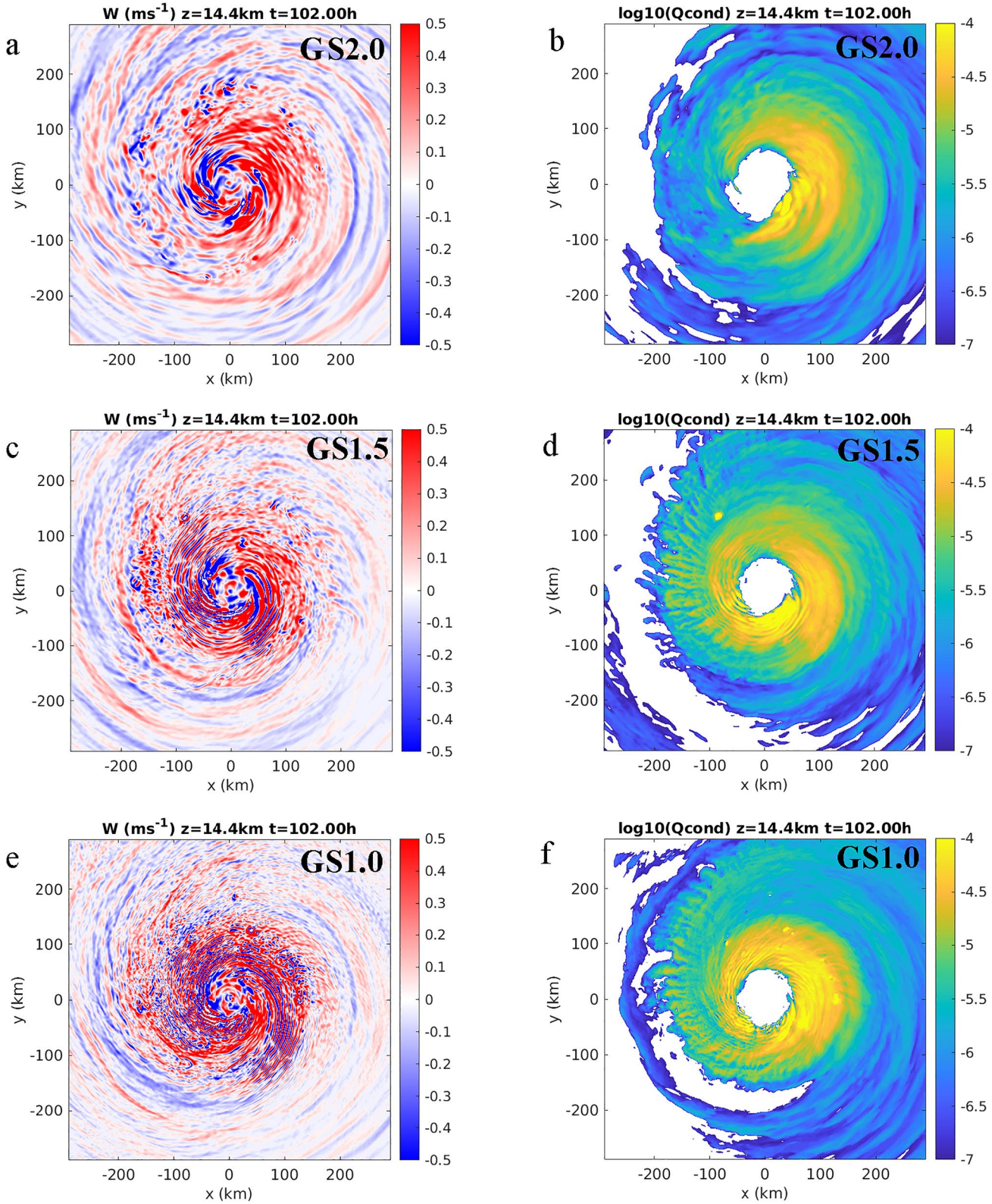

Figure 11. Horizontal slices of w and the logarithm of total condensate in the outflow region at z = 14.4 km: (a) w for GS2.0; (b) condensate for GS2.0; (c) w for GS1.5; (d) condensate for GS1.5; (e) w for GS1.0; (f) condensate for GS1.0.

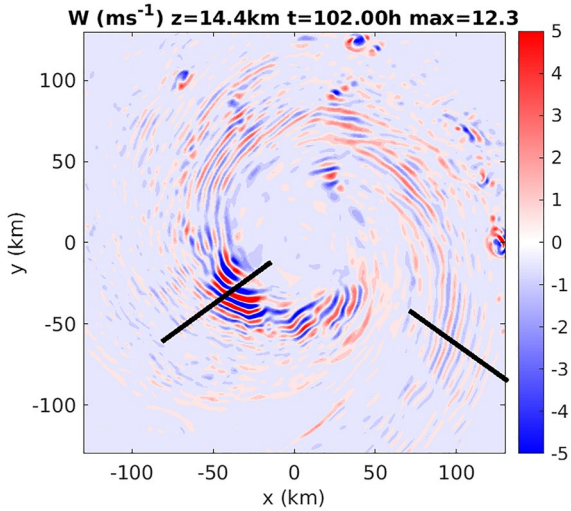

Figure 12. A close-up view of the same field as in Figure 11c, and with the color ranges increased to ±5 m s^{-1}. The black lines show the locations of radial-vertical cross sections of the fields shown in Figure 13.

r = 150 km. These propagate outwards with similar speeds to the w waves at 2.8 km. However, as the grid spacing decreases, a second class of spiral features in w becomes evident, which are the densely packed spirals closer to the center in the region from about r = 60 km to r = 120 km. Unlike the SGWs, these spirals do not propagate outward, but instead appear to rotate with the flow while remaining at approximately the same radius. (Note: A rotating spiral i.e., not moving outward still gives the *appearance* of moving outward, even though its features remain at constant radius.) An animation of Figure 11e is included as Movie S4.

Much of our knowledge of the upper-level flow in TCs comes from subjective and objective analyses of satellite images (Black & Anthes, 1971; Merrill & Velden, 1996; Oyama, 2017). As our simulations do not incorporate either shortwave or longwave radiation, we do not have a model variable that can be used to illustrate what a satellite would observe, for example, outgoing longwave radiation (OLR). However, in previous studies we found that the base 10 logarithm of the total condensate, that is, $\log_{10}(q_{\text{cond}})$, produces a field that looks remarkably like a satellite image (e.g., Figure 17 of Nolan, 2011). These are shown in the right column of Figure 11. These images also show similar, tightly spaced spirals of increased and decreased condensate in the same region. Low-wavenumber spirals are also apparent at farther distances, especially to the north and east.

To further distinguish these inner-core, outflow spirals from the SGWs, Figure 12 shows a closedup of the w field in Figure 11c with the color range expanded to −5 to +5 m s^{-1}. The inner spirals have much stronger vertical motions with values occasionally reaching 5 m s^{-1} and a maximum value of 12.3 m s^{-1}. The two black lines on these figures show the locations of radius-height cross sections that are shown in Figure 13. These locations were selected to highlight the two seemingly different types of slow-moving waves found in our simulations: short spiral waves at the top of the eyewall, and azimuthally longer waves that are further out in the outflow region. Figure 13 shows cross-sections of V_t, V_r, w, and $\log_{10}(q_{\text{cond}})$, along these lines. The waves appear to be shear instabilities, perhaps similar to stratified Kelvin-Helmholtz instability, that exist along the interface between the upper-level outflow and the compensating inflows above or below it. For the inner-core waves, the w values exceed 10 m s^{-1} in several of the updrafts. This is remarkably strong, given the large stratification in this region and the minimal water vapor available for condensation. The rotational motions of these large-amplitude waves are evident in the condensate field. For the waves in the outflow region, the amplitudes of the motions are not as large, but we can still see the oscillations in the horizontal wind fields and q_{cond}. The w perturbations show the classic structure of two sets of waves across a large gradient, phase shifted from each other for mutual amplification. Figure 13f also shows a very strong radial inflow layer directly below the primary outflow layer along this particular azimuth. This strong inflow may explain why the oscillating waves can be nearly stationary, as can be seen in Movie S4, even though they would appear to be embedded in 10–20 m s^{-1} of outflow.

As there have been very few direct observations of the upper-level outflow in the inner-cores of tropical cyclones, it is difficult to assess the realism of these vertical shears. Based on dropsondes released by high-altitude, uncrewed aircraft, Komaromi and Doyle (2017) show radial cross-sections of outflows in several hurricanes, which are very different from what is seen in Figure 13, with smaller values of V_r that peak hundreds of kilometers from the center. However, the number of their dropsondes within 100 km of the hurricane centers was quite small and the outflow regions above and immediately adjacent to the eyewalls are probably not resolved. Not surprisingly, the outflow structures shown in Figure 13 are consistent with many other numerical simulations, such as in Zhang et al. (2001), Wang and Xu (2010), and Wang et al. (2020). The compensating inflow structures shown in Figure 13 are even more intense than what appears in those studies because these fields are not azimuthally averaged (which is usually what is shown). The azimuthally averaged inflow, outflow, and tangential wind fields in these simulations are very similar to previous studies (not shown).

Figure 14a shows a Hovmöller diagram of the w fields at z = 14.4 km using FILT-W. Note that the left edge of the plot has been changed to r = 60 km. Here we can see a clear distinction between the inner spirals with their large amplitude and slow outward propagation and a transition to the rapidly propagating SGWs beyond r = 120 km.

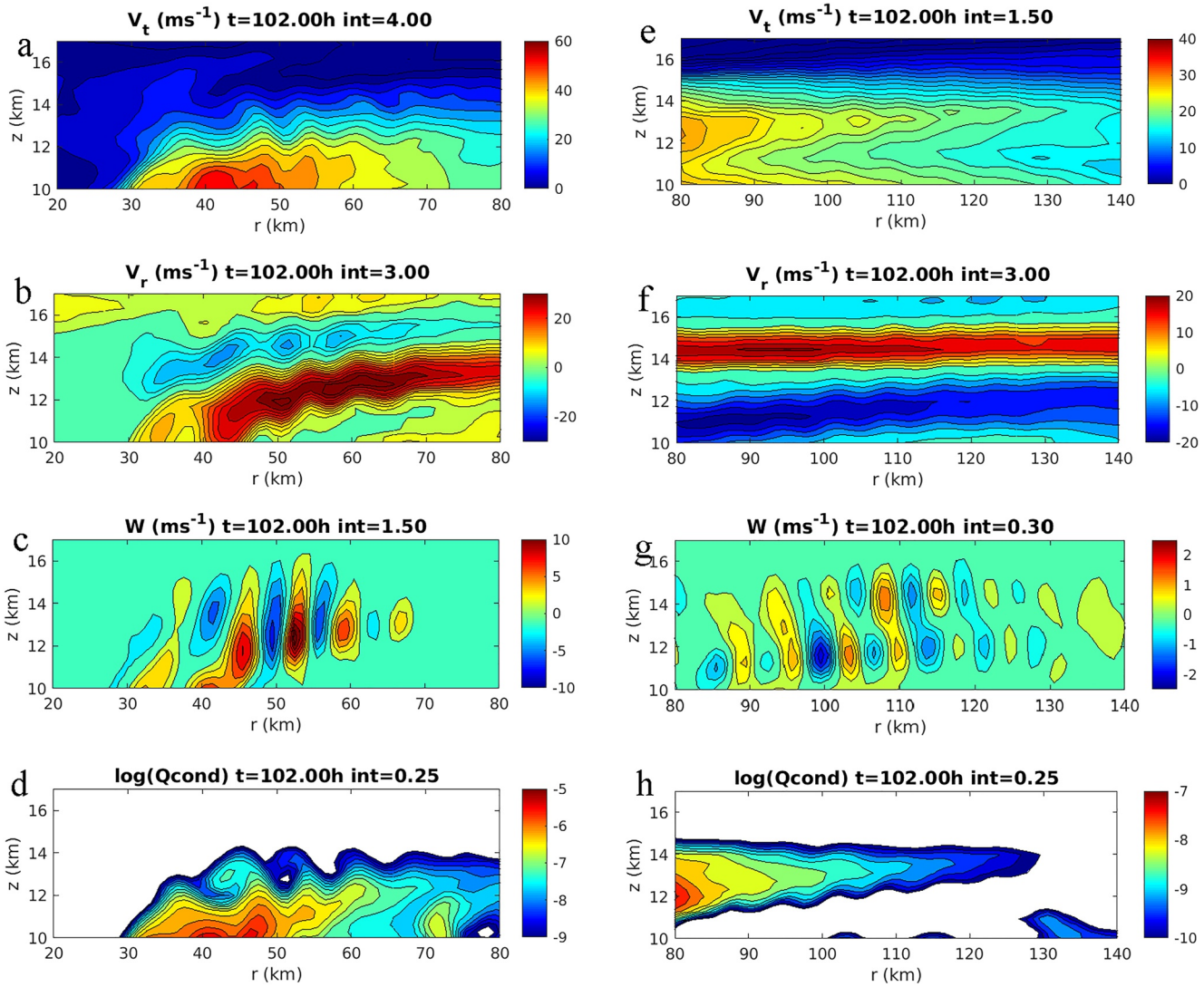

Figure 13. Slow-moving, large-amplitude waves in the outflow: (a) radius-height cross section of tangential velocity along the line on the left side of Figure 12; (b) radial velocity; (c) vertical velocity; (d) base 10 logarithm of total cloud condensate in kg kg^{-1}; (e)–(h), same but for the black line on the right side of Figure 12. Note that radius range and the color ranges are different for the two sets of plots.

We also performed the phase speed analysis for w at this altitude, and the result is shown in Figure 14b. For both the mean and for the individual quadrants, there is a shift of preferred phase speeds to higher values, from the range of 15–25 m s^{-1} to 20–30 m s^{-1}. Advection by the upper-level outflow does appear to increase the outward speeds of the SGWs, but not by as much as the actual outflow speed. Although our algorithm only measures one radial phase speed, it is apparent from Figure 14a that the phase speeds are decreasing with radius. This is due to the decreasing outflow speed that changes from 25 m s^{-1} around r = 100 km to 10 m s^{-1} at r = 300 km (not shown).

Returning to the slow-moving, inner spirals, some satellite images suggest that these structures may correspond to real features in tropical cyclones. Figure 15 shows two visible images of Typhoon Nepartak from the Himawari satellite at 0122 UTC and 0209 UTC on 6 July 2016. The storm was very symmetric at this time and the "best-track" intensity from the Joint Typhoon Warning Center is 145 knots (Bushnell & Falvey, 2016). Prominent spiral ridges just outside of the eye are visible in both images. An animation of the images over this time period, provided as Movie S5, show that the inner-core spiral cloud ridges do not propagate rapidly outward, consistent with what is seen in GS1.0. In the same animation, however, it is possible to discern larger-scale ripples or undulations in the cirrus field radiating rapidly away from the center. These are probably gravity waves.

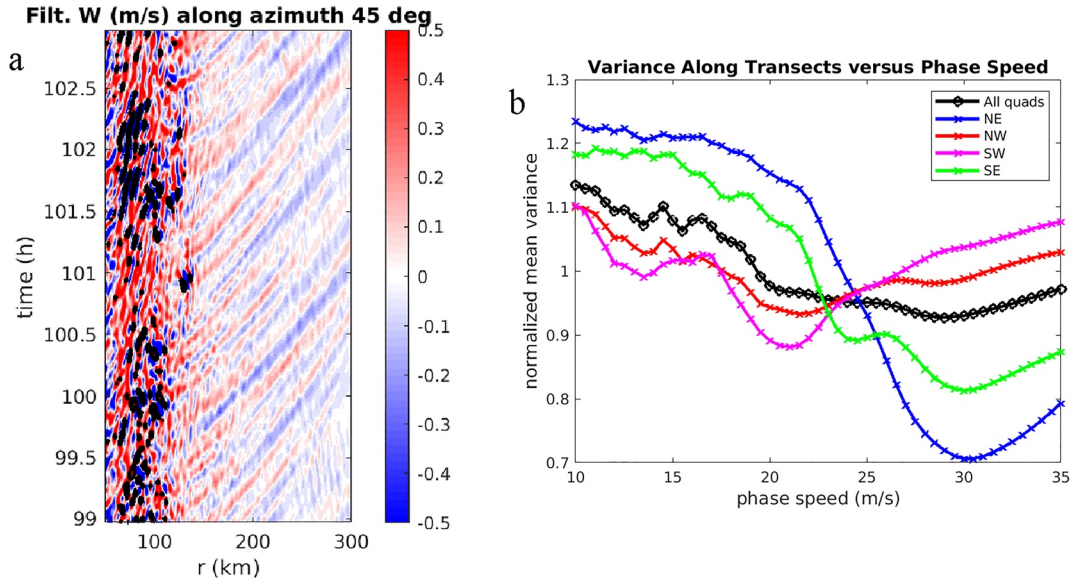

Figure 14. Radial propagation of w waves at $z = 14.4$ km in GS1.0: (a) radius-time Hovmöller diagram for w with FILT-W; (b) phase speed analysis for w waves in the outflow.

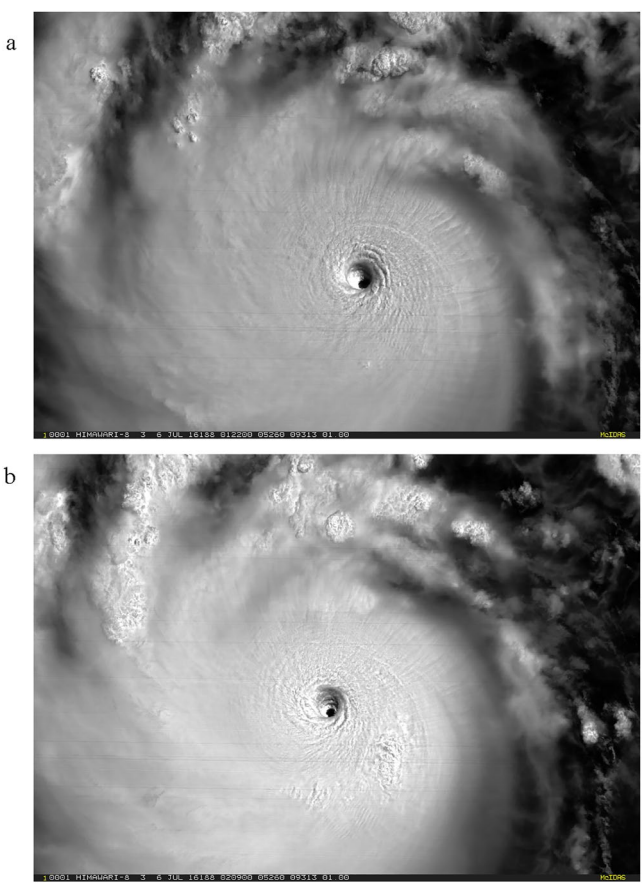

Figure 15. Visible images of Typhoon Nepartak (2016) taken by the Himawari satellite: (a) 0122 UTC 6 July; (b) 0209 UTC 6 July.

Returning to the spiral ridges, these are similar to the waves identified by Black (1983) from photographs taken from the Skylab Space Station. While NZ17 suggested that the features discussed by Black were evidence of gravity waves, it now appears that they are a distinct phenomenon.

Unfortunately, increasing either the horizontal or vertical resolution does not bring additional clarity to these upper level structures. Rather, as shown in Figure 16 for GS0.5 and L100, this only increases the areal coverage, diversity, and complexity of the slow-moving spiral features. For GS0.5, very fine-scale oscillations are evident in the w field over a broader area to the east and southeast of the center. However, Movie S6 and Movie S7 show that these smaller-scale structures move slowly while the low-wavenumber gravity waves pass through them. For L100, there are various patches of slow-moving waves, similar to the inner spiral waves, but at larger distances from the center. These appear, move, and dissipate slowly while the gravity waves radiate through them.

The exotic dynamics of these waves and the lack of convergence with increasing resolution are good reasons to be suspicious of their physical realism. And yet, the experienced observer of satellite images of TCs may recognize them as similar to patterns in the upper-level outflow that they have seen before. In our animation of Typhoon Nepartak, it is possible see short-wavelength waves that move slowly while the cirrus outflow and embedded gravity waves rapidly pass through them (these can be seen southeast of the center during the first half of the animation).

6. Summary and Conclusions

This paper explored the behaviors and dynamics of fine-scale SGWs that radiate from TCs. Since direct observations of these waves are very limited, our information comes from a series of idealized simulations of TCs with decreasing grid spacings of 2.0, 1.5, 1.0, and 0.5 km (GS2.0, GS1.5, GS1.0, and GS0.5). Two additional 1.0 km simulations were performed with half

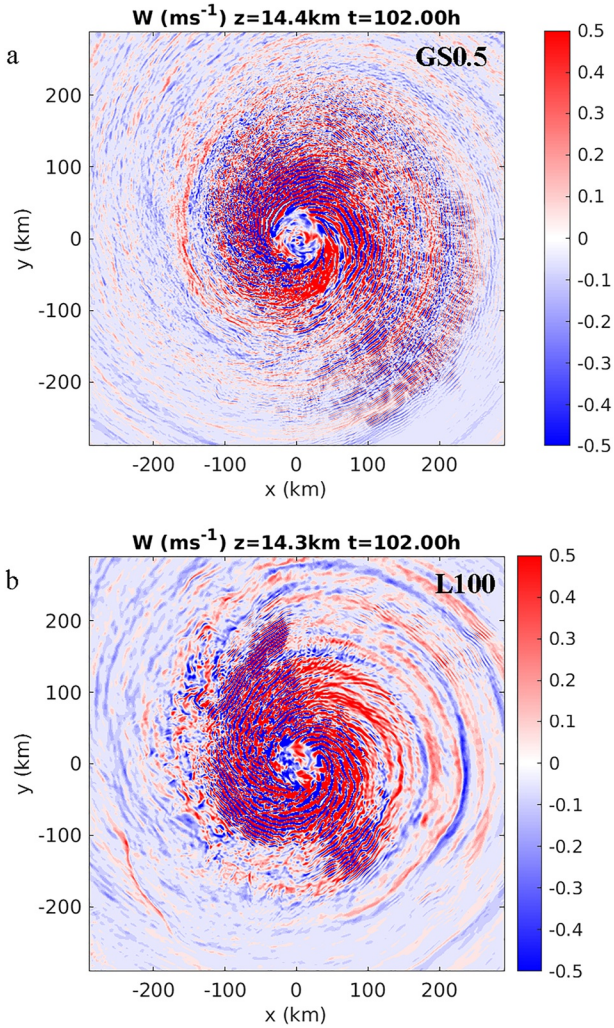

Figure 16. Horizontal slices of w near $z = 14.4$ km: (a) for GS0.5; (b) for L100.

and twice as many vertical levels (L25 and L100). The primary objective of this paper was to assess how the properties of the SGWs change as the grid spacing decreases (the resolution increases), and whether the properties of the waves were converging at the higher resolutions.

As in the previous studies of NZ17 and N20, we identified two classes of SGWs: small-scale w waves and larger-scale p waves which can be seen in the surface pressure field. Here, "scale" refers primarily to the radial wavelength, as both types of waves could be mostly represented as the sum of low wavenumbers in the azimuthal direction, for example, although the w waves were best captured by including up to $n = 64$. The p waves radiate outward with phase speeds of 50–70 m s^{-1}, and their radial wavelengths varied from about 100 km for GS2.0 down to 70 km for GS0.5. The radial scales and speeds of the p waves did appear converge as the grid spacing decreased to 1 km and less. The w waves radiate outward with phase speeds of 15–30 m s^{-1} and radial wavelengths ranging from 20 km for GS2.0–7 km for GS0.5. Although the radial scales do not appear to be converging, the results for GS1.0 and GS0.5 are approaching the observed wavelengths of 4–8 km as analyzed from in situ aircraft observations in NZ17.

The vertical structures of the waves were also investigated. The w waves are easily visible in vertical cross sections of the model output. The largest amplitudes occur in the upper-troposphere and appear to be embedded within the upper-level outflow. This was confirmed with an EOF analysis of time-height w data at fixed points which found that the first EOF had its peak amplitude at $z = 13$ km which oscillated with a time scale of about 20 min. The next two EOFs had higher vertical wavenumbers with peak amplitudes in the middle and lower troposphere. The first EOF of the pressure anomaly had its largest amplitude at the surface and oscillated with a time scale of about 70 min. For both increased horizontal and vertical resolution (GS0.5 and L100), the vertical structures of the w waves became narrower, while the EOFs of the p waves changed little. The vertical structure results reinforce our interpretation, proposed in NZ17 and N20, that there are two classes of SGWs radiating out of TC eyewalls: the shorter and slower w waves and the longer and faster p waves. The p waves are deeper while the w waves have more complicated vertical structures that probably evolve with time as they move outward.

Finally, we looked more closely at vertical motions in the upper-level outflow region, which is the part of the TC that is best observed by satellites. The upper-level signals of the SGWs are readily apparent in the "radiation region" outside the rainbands, where they move 5–10 m s^{-1} faster than the waves at 700 hPa, most likely due to radial advection by the outflow. However, plots and animations of the w field at $z = 14.4$ km show additional classes of slow-moving w waves. Some were persistently above and just outside of the eyewall, while others appeared in patches at larger distances from the center. Unlike the SGWs, these waves move slowly or may even be stationary at times. Although these behaviors are surprising, examination of satellite images and animations of TCs sometimes reveals similar features. The features in our simulations may be realistic, they may be poorly resolved representations of real phenomena, or they may be artifacts. Further study will be required to determine which is the case.

NZ17 and N20 speculated that it might be possible to infer the intensity or other properties of the source TC from measurements of the w or p waves. That would be difficult to assess explicitly from these simulations because they all have approximately the same intensity and inner-core size. In future work with these and other simulations, we hope to measure the decay in variance, and possibly changes in frequency, of the waves with distance from the TC center. With such information it may be possible to remotely estimate TC intensity from SGWs.

Data Availability Statement

Model output for the six simulations presented in this paper are available from the Zenodo repository at the following sites: for GS2.0, https://doi.org/10.5281/zenodo.5829550; for GS1.5, https://doi.org/10.5281/zenodo.5834340, for GS1.0, https://doi.org/10.5281/zenodo.5834877; for GS0.5, https://doi.org/10.5281/zenodo.5834761, for L25, https://doi.org/10.5281/zenodo.5834402; for L100, https://doi.org/10.5281/zenodo.5834531. The Himawari satellite images of Typhoon Nepartak are available at https://rammb.cira.colostate.edu/ramsdis/online/loop.asp?data_folder=loop_of_the_day/himawari/20160706000000%26number_of_images_to_display=100%26loop_speed_ms=100.

Acknowledgments
The WRF simulations used in this study were produced at the University of Miami Institute for Data Science and Computing (IDSC). The output from these simulations are archived and available and can be remotely transferred. D. Nolan was supported by the National Science Foundation under award AGS-1654831. Comments on earlier versions of the manuscript by J. Hlywiak and colleagues at the National Hurricane Center, and two anonymous reviewers, helped to improve the paper. We thank D. Lindsey for helping us to obtain the Himawari satellite images.

References

Aberson, S. D., Black, M. L., Black, R. A., Burpee, R. W., Cione, J. J., Landsea, C. W., & Marks, F. D., Jr. (2006). Thirty years of tropical cyclone research with the NOAA P-3 Aircraft. *Bulletin America Meteorology Social*, *87*(8), 1039–1055. https://doi.org/10.1175/BAMS-87-8-1039

Anthes, R. A. (1972). Development of asymmetries in a three-dimensional numerical model of the tropical cyclone. *Monthly Weather Review*, *100*(6), 461–476. https://doi.org/10.1175/1520-0493(1972)100<0461:doaiat>2.3.co;2

Anthes, R. A., Trout, J. W., & Rosenthal, S. L. (1971). Preliminary results from an asymmetric model of the tropical cyclone. *Monthly Weather Review*, *99*(10), 744–758. https://doi.org/10.1175/1520-0493(1971)099<0744:prfaam>2.3.co;2

Black, P. G. (1983). Tropical storm structure revealed by stereoscopic photographs from Skylab. *Advances in Space Research*, *2*(6), 115–124. https://doi.org/10.1016/0273-1177(82)90131-4

Black, P. G., & Anthes, R. A. (1971). On the asymmetric structure of the tropical cyclone outflow layer. *Journal of the Atmospheric Sciences*, *28*(8), 1348–1366. https://doi.org/10.1175/1520-0469(1971)028<1348:otasot>2.0.co;2

Braun, S. A., Montgomery, M. T., & Pu, Z. (2006). High-resolution simulation of Hurricane Bonnie (1998). Part I: The organization of eyewall vertical motion. *Journal of the Atmospheric Sciences*, *63*(1), 19–42. https://doi.org/10.1175/jas3598.1

Bushnell, J. M., & Falvey, R. J. (2016). Annual tropical cyclone report. Obtained from https://www.metoc.navy.mil/jtwc/products/atcr/2016atcr.pdf

Chow, K. C., & Chan, K. L. (2003). Angular momentum transports by moving spiral waves. *Journal of the Atmospheric Sciences*, *60*(16), 2004–2009. https://doi.org/10.1175/1520-0469(2003)060<2004:amtbms>2.0.co;2

Chow, K. C., Chan, K. L., & Lau, A. K. H. (2002). Generation of moving spiral bands in tropical cyclones. *Journal of the Atmospheric Sciences*, *59*(20), 2930–2950. https://doi.org/10.1175/1520-0469(2002)059<2930:gomsbi>2.0.co;2

Dai, Y., Majumdar, S. J., & Nolan, D. S. (2021). Tropical cyclone resistance to strong vertical wind shear. *Journal of the Atmospheric Sciences*, *78*(4), 1275–1293. https://doi.org/10.1175/JAS-D-20-0231.1

Dunion, J. P. (2011). Rewriting the climatology of the tropical North Atlantic and Caribbean Sea atmosphere. *Journal of Climate*, *24*(3), 893–908. https://doi.org/10.1175/2010JCLI3496.1

Dunion, J. P., Thorncroft, C. D., & Velden, C. S. (2014). The tropical cyclone diurnal cycle of mature hurricanes. *Monthly Weather Review*, *142*(10), 3900–3919. https://doi.org/10.1175/MWR-D-13-00191.1

Gall, R., Tuttle, J., & Hildebrand, P. (1998). Small-scale spiral bands observed in hurricanes Andrew, Hugo, and Erin. *Monthly Weather Review*, *126*(7), 1749–1766. https://doi.org/10.1175/1520-0493(1998)126<1749:sssboi>2.0.co;2

Hendricks, E. A., Schubert, W. H., McNoldy, B. D., & Fulton, S. R. (2010). Spontaneous-adjustment emission of inertia-gravity waves by unsteady vortical motion in the hurricane core. *Quarterly Journal of the Royal Meteorological Society*, *136*(647), 537–548. https://doi.org/10.1002/qj.547

Hlywiak, J., & Nolan, D. S. (2019). The influence of oceanic boundary layers on tropical cyclone intensity as determined through idealized, coupled numerical simulations. *Journal of Physical Oceanography*, *49*(7), 1723–1745. https://doi.org/10.1175/JPO-D-18-0267.1

Hong, S. Y., & Lim, J. O. J. (2006). The WRF single-moment 6-class microphysics scheme (WSM6). *Journal of the Korean Meteorological Society*, *42*, 129–151.

Hong, S. Y., Noh, Y., & Dudhia, J. (2004). A new vertical diffusion package with an explicit treatment of entrainment processes. *Monthly Weather Review*, *134*(9), 2318–2341. https://doi.org/10.1175/mwr3199.1

Klemp, J. B., Dudhia, J., & Hassiotis, A. D. (2008). An upper-level gravity wave absorbing layer for NWP applications. *Monthly Weather Review*, *136*(10), 3987–4004. https://doi.org/10.1175/2008MWR2596.1

Komaromi, W. A., & Doyle, J. D. (2017). Tropical cyclone outflow and warm-core structure as revealed by HS3 dropsonde data. *Monthly Weather Review*, *145*, 1339–1359. https://doi.org/10.1175/MWR-D-16-0172.1

Kurihara, Y., & Tuleya, R. E. (1974). Structure of a tropical cyclone developed in a three-dimensional model. *Journal of the Atmospheric Sciences*, *31*(4), 893–919. https://doi.org/10.1175/1520-0469(1974)031<0893:soatcd>2.0.co;2

Liu, Y., Zhang, D.-L., & Yau, M. K. (1997). A multiscale numerical study of Hurricane Andrew (1992). Part I: An explicit simulation. *Monthly Weather Review*, *125*(12), 3073–3093. https://doi.org/10.1175/1520-0493(1997)125<3073:amnsoh>2.0.co;2

Merrill, R. T., & Velden, C. S. (1996). A three-dimensional analysis of the outflow of Super-typhoon Flo (1990). *Monthly Weather Review*, *124*(1), 47–63. https://doi.org/10.1175/1520-0493(1996)124<0047:atdaot>2.0.co;2

Moon, Y., & Nolan, D. S. (2010). Do gravity waves transport angular momentum away from hurricanes? *Journal of the Atmospheric Sciences*, *67*(1), 117–135. https://doi.org/10.1175/2009jas3088.1

Moon, Y., & Nolan, D. S. (2015a). Spiral rainbands in a numerical simulation of Hurricane Bill (2009). Part I: Structures and comparisons to observations. *Journal of the Atmospheric Sciences*, *72*(1), 164–190. https://doi.org/10.1175/jas-d-14-0058.1

Moon, Y., & Nolan, D. S. (2015b). Spiral rainbands in a numerical simulation of Hurricane Bill (2009). Part II: Propagation of inner rainbands. *Journal of the Atmospheric Sciences*, *72*(1), 191–215. https://doi.org/10.1175/jas-d-14-0056.1

Morrison, H. (2016). Impacts of updrafts size and dimensionality on the perturbation pressure and vertical velocity in cumulus convection. Part I: Simple, generalized analytic solutions. *Journal of the Atmospheric Sciences*, *73*(4), 1441–1454. https://doi.org/10.1175/JAS-D-15-0040.1

Morrison, I., Businger, S., Marks, F., Dodge, P., & Businger, J. A. (2005). An observational case for the prevalence of roll vortices in the hurricane boundary layer. *Journal of the Atmospheric Sciences*, *62*(8), 2662–2673. https://doi.org/10.1175/jas3508.1

Nguyen, L. T., Molinari, J., & Thomas, D. (2014). Evaluation of tropical cyclone center identification methods in numerical models. *Monthly Weather Review*, *142*(11), 4326–4339. https://doi.org/10.1175/MWR-D-14-00044.1

Nolan, D. S. (2005). Instabilities in hurricane-like boundary layers. *Dynamics of Atmospheres and Oceans*, *40*(3), 209–236. https://doi.org/10.1016/j.dynatmoce.2005.03.002

Nolan, D. S. (2011). Evaluating environmental favorableness for tropical cyclone development with the method of point-downscaling. *Journal of Advances in Modeling Earth Systems*, *3*(8), M08001. https://doi.org/10.1029/2011MS000063

Nolan, D. S. (2020). An investigation of spiral gravity waves radiating from tropical cyclones using a linear, nonhydrostatic model. *Journal of the Atmospheric Sciences*, *77*(5), 1733–1759. https://doi.org/10.1175/jas-d-19-0259.1

Nolan, D. S., Atlas, R., Bhatia, K. T., & Bucci, L. R. (2013). Development and validation of a hurricane nature run using the joint OSSE nature run and the WRF model. *Journal of Advances in Modeling Earth Systems*, *5*(2), 382–405. https://doi.org/10.1002/jame.20031

Nolan, D. S., & McGauley, M. G. (2012). Tropical cyclogenesis in wind shear: Climatological relationships and physical processes. In K. Oouchi & H. Fudeyasu (Eds.), *Cyclones: Formation, triggers, and control* (pp. 1–34). Nova Science Publishers.

Nolan, D. S., & Zhang, J. A. (2017). Spiral gravity waves radiating from tropical cyclones. *Geophysical Research Letters*, *44*(8), 3924–3931. https://doi.org/10.1002/2017GL073572

Nolan, D. S., Zhang, J. A., & Uhlhorn, E. W. (2014). On the limits of estimating the maximum wind speeds in hurricanes. *Monthly Weather Review*, *142*(8), 2814–2837. https://doi.org/10.1175/MWR-D-13-00337.1

O'Neill, M. E., Perez-Betancourt, D., & Wing, A. A. (2017). Accessible environments for diurnal-period waves in simulated tropical cyclones. *Journal of the Atmospheric Sciences*, *74*(8), 2489–2502. https://doi.org/10.1175/JAS-D-16-0294.1

Onderlinde, M. J., & Nolan, D. S. (2016). Tropical-cyclone-relative environmental helicity and the pathways to intensification of tropical cyclones in shear. *Journal of the Atmospheric Sciences*, *73*(2), 869–690. https://doi.org/10.1175/jas-d-15-0261.1

Oyama, R. (2017). Relationship between tropical cyclone intensification and cloud-top outflow revealed by upper-tropospheric atmospheric motion vectors. *Journal of Applied Meteorology and Climatology*, *10*, 2801–2819. https://doi.org/10.1175/JAMC-D-17-0058.1

Potter, H., Graber, H. C., Williams, N. J., Collins, C. O., III, Ramos, R. J., & Drennan, W. M. (2015). In situ measurements of momentum fluxes in typhoons. *Journal of the Atmospheric Sciences*, *72*(1), 104–118. https://doi.org/10.1175/jas-d-14-0025.1

Press, W. H., Teulosky, S. A., Vetterling, W. T., & Flannery, B. P. (1992). *Numerical recipes in fortran* (p. 963). Cambridge University Press.

Rios-Berrios, R. (2020). Impacts of radiation and cold pools on the intensity and vortex tilt of weak tropical cyclones interacting with vertical wind shear. *Journal of the Atmospheric Sciences*, *77*(2), 669–689. https://doi.org/10.1175/JAS-D-19-0159.1

Rogers, R., Chen, S. S., Tenerelli, J. E., & Willoughby, H. E. (2003). A numerical study of the impact of vertical shear on the distribution of rainfall in Hurricane Bonnie (1998). *Monthly Weather Review*, *131*(8), 1577–1599. https://doi.org/10.1175//2546.1

Rotunno, R., Chen, Y., Wang, W., Davis, C., Dudhia, J., & Holland, G. J. (2009). Large-eddy simulation of an idealized tropical cyclone. *Bulletin America Meteorology Social*, *90*(12), 1783–1788. https://doi.org/10.1175/2009BAMS2884.1

Schecter, D. A. (2008). The spontaneous imbalance of an atmospheric vortex at high Rossby number. *Journal of the Atmospheric Sciences*, *65*(8), 2498–2521. https://doi.org/10.1175/2007jas2490.1

Skamarock, W. C. (2004). Evaluating mesoscale NWP models using kinetic energy spectra. *Monthly Weather Review*, *132*(12), 3019–3032. https://doi.org/10.1175/MWR2830.1

Wang, S., Smith, R. K., & Montgomery, M. T. (2020). Upper-troposphereic inflow layers in tropical cyclones. *Quarterly Journal of the Royal Meteorological Society*, *146*(732), 3466–3487. https://doi.org/10.1002/qj.3856

Wang, Y., & Xu, J. (2010). Energy production, frictional dissipation, and maximum intensity of a numerically simulated tropical cyclone. *Journal of the Atmospheric Sciences*, *67*(1), 97–116. https://doi.org/10.1175/2009JAS3143.1

Zhang, D.-L., Liu, Y., & Yau, M. K. (2001). A multiscale numerical study of Hurricane Andrew (1992). Part IV: Unbalanced flows. *Monthly Weather Review*, *129*(1), 92–107. https://doi.org/10.1175/1520-0493(2001)129<0092:amnsoh>2.0.co;2

Zhang, F., & Tao, D. (2013). Effects of vertical wind shear on the predictability of tropical cyclones. *Journal of the Atmospheric Sciences*, *70*(3), 975–983. https://doi.org/10.1175/JAS-D-12-0133.1